TERMINAL DOPPLER WEATHER RADAR BOUNDARY LAYER OBSERVATIONS DURING A SUMMER HIGH OZONE PERIOD IN COMPLEX TERRAIN

by

Aaron Caleb McCutchan

A thesis submitted to the faculty of
The University of Utah
in partial fulfillment of the requirements for the degree of

Master of Science

Department of Atmospheric Sciences

The University of Utah

December 2023

The University of Utah Graduate School

STATEMENT OF THESIS APPROVAL

The thesis of **Aaron Caleb McCutchan**

has been approved by the following supervisory committee members:

John D. Horel	, Chair	**08/30/2023**
		Date Approved
Sebastian Wilhelm Hoch	, Member	**08/30/2023**
		Date Approved
Kevin Perry	, Member	**08/31/2023**
		Date Approved

and by **Brenda B. Bowen**, Chair of

the Department of **Atmospheric Sciences**

and by **Darryl P. Butt**, Dean of The Graduate School.

ABSTRACT

An exceptional heat wave led to high ozone concentrations in northern Utah during 29 August 2022 - 7 September 2022. Eight-hour average ozone concentrations exceeded National Ambient Air Quality Standards (NAAQS) during five of the ten days within the Salt Lake Valley (SLV) and to its north in the urban corridor bordering Farmington Bay Playa (FBP). A team from the University of Utah (UU) conducted a field study over summer 2022 involving surface-based observations and remote sensors in and around FBP to facilitate greater understanding of ozone transport to nearby urban areas. Time-height sections of velocity volume processing (VVP) and reflectivity range-defined quasi-vertical profile (RD-QVP) retrievals were developed for TSLC, the Terminal Doppler Weather Radar (TDWR) for Salt Lake City (SLC) International Airport located on the eastern edge of FBP. Time-height sections are compared to observations from permanently installed regulatory and temporary field study sensors to assess the daily development of the boundary layer and potential impacts on ozone concentrations.

Well defined vertical wind shear zones within 500 m of the surface help define the top of the morning stable boundary layer. Tracking the growth of the convective boundary layer (CBL) is possible until mid-afternoon when the CBL rapidly deepens to >2000 m above ground level. The rapid increases in CBL height and associated vertical mixing contribute to sharp decreases in near-surface ozone concentrations on days when ozone concentrations aloft are substantially lower. Flow in the layer aloft during the morning hours transports high ozone present the evening before away from the urban centers and advects lower concentration background values into the region. This process is most efficient when flow aloft is easterly, away from the tallest terrain barriers, and least efficient when the flow is westerly, toward the tallest terrain barriers. Ozone concentrations on the west side of the FBP and SLV basins are often influenced by lake breezes originating from the Gilbert Bay arm of the Great Salt Lake.

This work is dedicated to the people who made it possible:

Larry and Tracy, who tried

Bethany and Diana, who cared

Ebby and Roo, who kept me company

Kayley, who never gave up

Nick, who shared the vision

Ted and Jen, who created space when I was suffocating

Emma and Charles, my first found family

Terry and Alexander, who opened the door

Bekah, who lightened the load

Christiaan, who taught life is more than the tornado

Jay, who shaped the path

Jackson, Jamie, Arthur, and Ash, who had the courage to say we exist

Mark and Joebob, who reminded me to make mistakes

John, who took a chance

Ariel, who saw me first

Kim, who showed life is viable

Grace, who proved love reincarnates

Michell, Jacob, and Heather, who listened

Stevie, who got me to stop saying it's impossible

Bug, who drifted through uncertainty at my side

Kaitlyn, Meg, Ray, and Sheila, who stayed

Katherine, who turned the tide in a long battle

Adam, Jack, and Ryan, who carried me through the darkest moments

Sebastian, who kept faith in me when I lost it

I would not be here without them.

CONTENTS

LIST OF FIGURES

ACKNOWLEDGEMENTS

This work was possible due to the computing resources provided by the University of Utah's Center for High Performance Computing. The Python ARM Radar Toolkit (Py-ART) library was used extensively for radar data processing. Funding for this project was provided by the Utah Division of Air Quality and the NOAA/National Weather Service Collaborative Science, Technology, and Applied Research (CSTAR) Program, Award NA20NWS468046.

CHAPTER 1

INTRODUCTION

During late August 2022, a ridge responsible for a record-setting heat wave in the Pacific Northwest positioned its axis over Utah, creating impacts in the region through the middle of September. Temperatures were abnormally warm in Salt Lake City (SLC), and eight-hour average ozone concentrations ($\overline{O_3}$) exceeded the National Ambient Air Quality Standard (NAAQS) set by the Environmental Protection Agency (EPA) many days between 29 Aug 2022 and 7 Sep 2022, and the remaining days nearly exceeded the standard. Labor Day was observed on 5 Sep 2022, thus this period is referred to as the Labor Day period (LDP). A University of Utah (UU) team was in the midst of a small field study (Horel et al. 2023) and deployed ozone monitoring sensors and other equipment near the Farmington Bay Playa (FBP), so named after the arm of the Great Salt Lake (GSL) that used to fill the region to the east of Antelope Island. These field observations combined with permanently installed sensors and boundary layer observations from a Terminal Doppler Weather Radar (TDWR) covering Salt Lake City International Airport (TSLC) allow detailed analysis of meteorological processes that contributed to poor air quality during this event.

High tropospheric ozone concentrations constitute an environmental hazard, damaging vegetation (Van Dingenen et al. 2009; Clifton et al. 2020), increasing hospitalizations from acute exposure, and causing or exacerbating chronic health conditions with repeated exposure (Hubbell et al. 2005; Fann et al. 2012; Sousa et al. 2013). Ozone pollution is complex, relying on a myriad of factors including precursor chemical concentrations, insolation, photochemical reactions, boundary layer processes, and transport by winds on all scales. While weather cannot be regulated, it does play a critical role in shaping the impacts of emissions. Thus, greater understanding of the impacts of atmospheric conditions on ozone concentrations may help development of effective regulations.

Ozone is presently regulated in terms of $\overline{O_3}$, with NAAQS stating $\overline{O_3}$ is not to exceed 70 ppb. Salt Lake and Davis counties, the urban regions adjacent to FBP, are presently moderate non-attainment zones. The EPA has been considering lowering this standard to 65 ppb. For the purposes of this study, days with $\overline{O_3}$ exceeding 70 ppb are referred to as exceedance events, and days exceeding 65 ppb as near exceedance events. The Utah Division of Air Quality (DAQ) has a network of sensors spanning the state to monitor criteria pollutants, including ozone.

Boundary layer processes influence observed ozone concentrations and generally follow a diurnal cycle in dry, quiescent conditions like those in the LDP (Stull 1988). The nocturnal stable boundary layer begins eroding after sunrise in response to radiative heating of the surface below. Heat transfers into the lowest atmospheric layer via conduction from the surface and forms a shallow superadiabatic layer. This superadiabatic layer introduces instability which creates a turbulent, dry-adiabatic convective boundary layer (CBL). On top is an entrainment zone, mixing air aloft into the CBL below. As surface heating continues during the day, turbulent vertical mixing increases CBL depth until sunset. At that time, turbulence wanes, radiative cooling dominates, and a stable boundary layer reforms near the surface. The remnants of the well-mixed CBL mostly unaffected by the cooling form the residual layer (RL).

Photochemical ozone production shares a similar dependence upon solar radiation. Ozone is not a primary pollutant, rather the byproduct of volatile organic carbons (VOCs) being oxidized by nitrous oxides (NO_x) in the presence of sunlight, with both reactants sourced from urban emissions (Seinfeld and Pandis 2016). These reactions become more efficient at high ambient air temperatures (Pusede et al. 2015; Coates et al. 2016) and depend on the amount of incoming solar radiation, with production being maximized at solar noon (Baier et al. 2015).

Precursor chemical species initially trapped within the shallow CBL help to focus ozone production near the surface. During the morning hours, ozone production tends to overcome the diluting effect of entraining relatively cleaner RL air into the CBL and increase ozone concentrations. After solar noon, when ozone production begins decreasing and the CBL is deep, the diluting effect tends to dominate, causing ozone concentrations

near the surface to decrease slowly until sunset (Kaser et al. 2017). Nearly constant ozone concentrations in height will result from a neutrally stratified, turbulent CBL, becoming the RL after sunset. After sunset, titration (Seinfeld and Pandis 2016), deposition (Clifton et al. 2020), and scavenging by halide species (Simpson et al. 2007; Seinfeld and Pandis 2016) contribute to decreases in near-surface ozone. These effects are reduced in the RL, thus the surface tends to experience more ozone concentration extremes than layers aloft (Kaser et al. 2017).

Elevated ozone and precursor concentrations in the mid and upper troposphere contribute to increased $\overline{O_3}$ in many cities within the Intermountain West (Brodin et al. 2010). Downslope and down-valley winds transport background ozone aloft to basin floors at night (Liu et al. 1992; Jaffe 2011; Chow et al. 2013; Horel et al. 2016), while upslope flows advect higher ozone concentrations from urban valleys up nearby slopes and canyons. This effect is most apparent during quiescent periods (Chow et al. 2013).

Lake and sea breezes are another thermally driven circulation that can influence ozone transport. These form in response to the greater thermal inertia of bodies of water, which cause the boundary layer above the water surface to become less dense more slowly than the adjacent boundary layer over land under the influence of solar radiation. In situations where synoptic forcing is weak, these can propagate onshore from above the lake surface as a density current, with a leading lake breeze front that may inject surface ozone into higher layers (Zumpfe and Horel 2007; Crosman and Horel 2010). Similar circulations can happen off of playa surfaces due to the higher thermal inertia of playa surfaces compared to surrounding areas (Massey et al. 2017). Lake breezes are well known to influence surface ozone concentrations. In some cases, convergence zones along a lake breeze front concentrate ozone, which can then be transported along as the lake breeze propagates or lead to high ozone concentrations in an area where it is stalled (Banta et al. 2011; Goldberg et al. 2014; Wentworth et al. 2015; Blaylock et al. 2017). Additionally, ozone in the boundary layer above the lake is frequently different than over land due to generally shallower CBL depths and chemistry differences which cause the lake breeze to act as a source or sink of ozone.

The SLV and FBP basins provide a unique natural laboratory to monitor the interplay of thermally driven flows and boundary layer phenomena with ozone (Fig. 1.1). SLV and FBP basins are located at an elevation of roughly 1300 m above sea level. The east boundary of these basins is the Wasatch Mountains, ranging in height up to 3000 m above the basin floor. The SLV is bounded to the west by the Oquirrh Mountains (peak height 2700 m) and to the south by the Traverse Mountains. To the north of the Oquirrh Mountains lies Antelope Island (peak height approximately 700 m), which marks the westernmost extent of FBP. The Jordan River flows through the center of both basins along a north-south axis, entering FBP thorugh wetlands on its southern perimeter and connecting to the main body of the GSL north of Antelope Island via small residual flow.

Mornings during quiescent periods are often dominated by southerly atmospheric flow over SLV and western FBP (Zumpfe and Horel 2007) along with an easterly jet that forms between the mouth of Weber Canyon and the northern end of Antelope Island (Chrust et al. 2013). Daytime heating reverses the thermally driven flows responsible, and flow becomes predominantly northerly while the Weber Canyon jet dissipates. Lake breezes from Gilbert Bay enter the SLV in the gap between Antelope Island and the Oquirrh mountains. The lake breeze begins propagating to the southeast during midday and often becomes oriented from east to west across the axis of SLV. If synoptic southerly flow is present that opposes the northerly lake breeze driven flow, the area of frontogenesis forming the lake breeze front that would otherwise be dissipated by turbulence over land is maintained and propagates south through the SLV over the course of the afternoon (Zumpfe and Horel 2007; Blaylock et al. 2017).

Clear air returns from weather radars can be used to track lake breezes (Wentworth et al. 2015; Blaylock et al. 2017). Work has been done characterizing the nature of clear air scatterers tracing the flow for these observations. There are broadly two categories, Bragg and biota, and are most easily differentiated using polarimetric data. Bragg scattering comes from isotropic turbulence (Doviak and Zrnic 1993), thus has a differential reflectivity (Z_{DR}) near zero. On the other hand, biota tend to be much wider than tall when in flight and appear anisotropic to the radar, with high Z_{DR} (Zrnic and Ryzhkov 1998). Unfortunately without polarimetric data, signals from both are nearly identical and differentiation is

impossible (Banghoff et al. 2018). While the composition of the scatterers cannot be derived, reflectivity layer depth depends upon boundary layer depth and can be used to track CBL development (Heinselman et al. 2009; Banghoff et al. 2018). Regardless of type, motion of scatterers did not significantly bias wind estimates in this study.

The 2022 summer ozone project (Horel et al. 2023) was a successor to the 2015 summer ozone project (Horel et al. 2016). In the earlier study, thermally driven circulations had a significant impact on local ozone concentrations and appeared to be acting to concentrate ozone in the urban corridor between FBP and the Wasatch Front. The summer 2022 study deployed ceilometers, sodars, and meteorological and ozone monitoring equipment in this region with the goal of understanding transport out of the FBP wetlands into the nearby urban corridor. Radar retrievals applied to the TDWR near FBP provide additional information about the boundary layer growth, structure, and flows.

The objectives of this study are:

1. Understand the limitations of and optimize radar retrievals for use on TDWR radars located in complex terrain;
2. Observe the transition from the morning stable boundary layer to the CBL during LDP using TSLC plan view images and time height profiles of wind speed and direction reported every 6 min at 50 m vertical resolution;
3. Compare observed CBL development to observed ozone concentrations.

The next section (Chapter 2) introduces three data sets: the summer ozone study instrumentation, TDWR, and High Resolution Rapid Refresh (HRRR) model. The following Chapter 3 gives a detailed description of the retrievals applied to TSLC, with special care given to constraints arising from the radar's location in complex terrain. Then, Chapter 4 provides a broad overview of synoptic conditions during LDP before going into conditions during each day. Chapter 5 summarizes the work and provides potential directions for future research.

Figure 1.1: Major geographic features of Salt Lake Valley and Farmington Bay Playa basins.

CHAPTER 2

DATASETS

2.1 Summer 2022 Ozone Study

The 2022 summer ozone study conducted by a UU team (Horel et al. 2023) was designed to validate the hypothesis put forward by the 2015 summer ozone study that FBP was a significant source of ozone for the nearby urban corridor using a network of surface observations and surface based remote sensors (Fig. 2.1). DAQ has a number of permanently installed regulatory grade ozone monitors around the SLV and FBP basins. Research grade 2B Technologies ozone monitors were placed at UUPYA, USDR4, and UFD15. Tower mounted meteorological sensors including wind and temperature were available at UUPYA and UFD15. Sodars capable of observing winds in the lowest 100 m were sited at USDR1, USDR4, and USDR5. These stations were set up along the edge of FBP to monitor transport near the region while UUPYA monitors conditions on the playa. Ozone reported at DAQ sites are analyzed using one-hour averages. For comparison, a one-hour running mean smoother was applied to ozone concentrations reported every 5 minutes at UU sites.

2.2 NEXRAD and TDWR Radar Networks

This study makes use of TSLC, the TDWR for SLC International Airport, located on the east side of FBP (Fig. 2.1). The Federal Aviation Administration operates TDWR radars to provide higher resolution coverage near major airports that frequently experience strong wind shear. These TDWR radars supplement observations from the National Oceanic and Atmospheric Administration (NOAA) next generation weather radar (NEXRAD) network (NOAA NCEI 2023a,b). Table 2.1 provides technical specifications for NEXRAD and TDWR. Data from both radar networks are archived publicly via cloud providers as part of the NOAA Open Data Dissemination Program (NOAA Information Technology 2023). Level-2

data from TSLC is available Sep 2020 - present. KMTX, the SLC NEXRAD radar, is located on Promontory Point, a mountain to the north of SLC, and scans above the GSL basin. TSLC is on the basin floor and subject to significant terrain beam blockage (Fig. 2.2). Only horizontal polarization (single-pol) products are available from TSLC to observe the boundary layer. Thus Z_{DR} used by Banghoff et al. (2018) is unavailable. The Volume Coverage Pattern (VCP) for TSLC is determined automatically, switching to hazard mode upon detection of meteorological 20 dBZ reflectivity echoes or wind shear near the airport (NOAA NCEI 2023b). TDWR dealiasing is handled at the instrument before transmission to end users (Cho 2005, 2010). Since wind speeds during the study period were generally below the lowest possible TDWR aliasing velocity of 10 $m\ s^{-1}$ (NOAA NCEI 2023b), dealiasing errors are not a concern here.

2.3 High Resolution Rapid Refresh (HRRR) Model

The HRRR model is a regional, operational forecast model managed by NOAA's National Centers for Environmental Prediction (NCEP). Designed for use across the continental United States and Alaska, the HRRR model is a convection-allowing, cloud-resolving forecast model that runs hourly over the CONUS and once every three hours over Alaska (Benjamin et al. 2016; Dowell et al. 2022; James et al. 2022). The HRRR provides users with frequent, real-time, high-resolution, deterministic analyses and forecasts. Such products aid in many short–range applications ranging from general monitoring of atmospheric conditions, convective and stratiform cloud development, prediction of various severe weather types, wind circulations, and wildfire smoke plume prediction (James et al. 2022).

Introduced in September 2014 as a complement to the 13-km Rapid Refresh (RAP) model, the HRRR model assimilates initial condition data provided by the RAP (Benjamin et al. 2016; Dowell et al. 2022) and conventional observations and delivers a four times higher resolution in both space and time offering horizontal resolutions of 3-km grid spacing in addition to over 50 vertical levels (NOAA NCEP EMC 2021). Reflectivity data from both NEXRAD and TDWR are assimilated via multi-radar multi-sensor (MRMS) products (Smith et al. 2016; Zhang et al. 2016; Dowell et al. 2022). NEXRAD radial velocity and velocity azimuth display (VAD) products are also assimilated in RAP, but NEXRAD dual-pol and

TDWR products are not directly assimilated (Liu et al. 2016; Dowell et al. 2022). Archived access to the high-resolution model output is currently available through Amazon Web Services and Google's Cloud Platform (Gowan et al. 2022; Dowell et al. 2022).

Table 2.1: Operating characteristics of Next Generation Weather Radar (NEXRAD) and Terminal Doppler Weather Radar (TDWR) network radars (NOAA NCEI 2023a,b). Scan update times are approximate.

Characteristic	TDWR	NEXRAD
Wavelength	C-Band (5 cm)	S-Band (10 cm)
Antenna Polarization(s)	Horizontal only	Horizontal and vertical
Gate Length	150 m	250 m
Unambiguous Range	90 km	230 km
Clear Air Mode Volume Scan Time	6 min	12 min
Hazard Mode Volume Scan Time	3 min	4 min
Aliasing velocity	10 - 15 $m\ s^{-1}$	32 $m\ s^{-1}$
Beamwidth	0.5°	1.25°

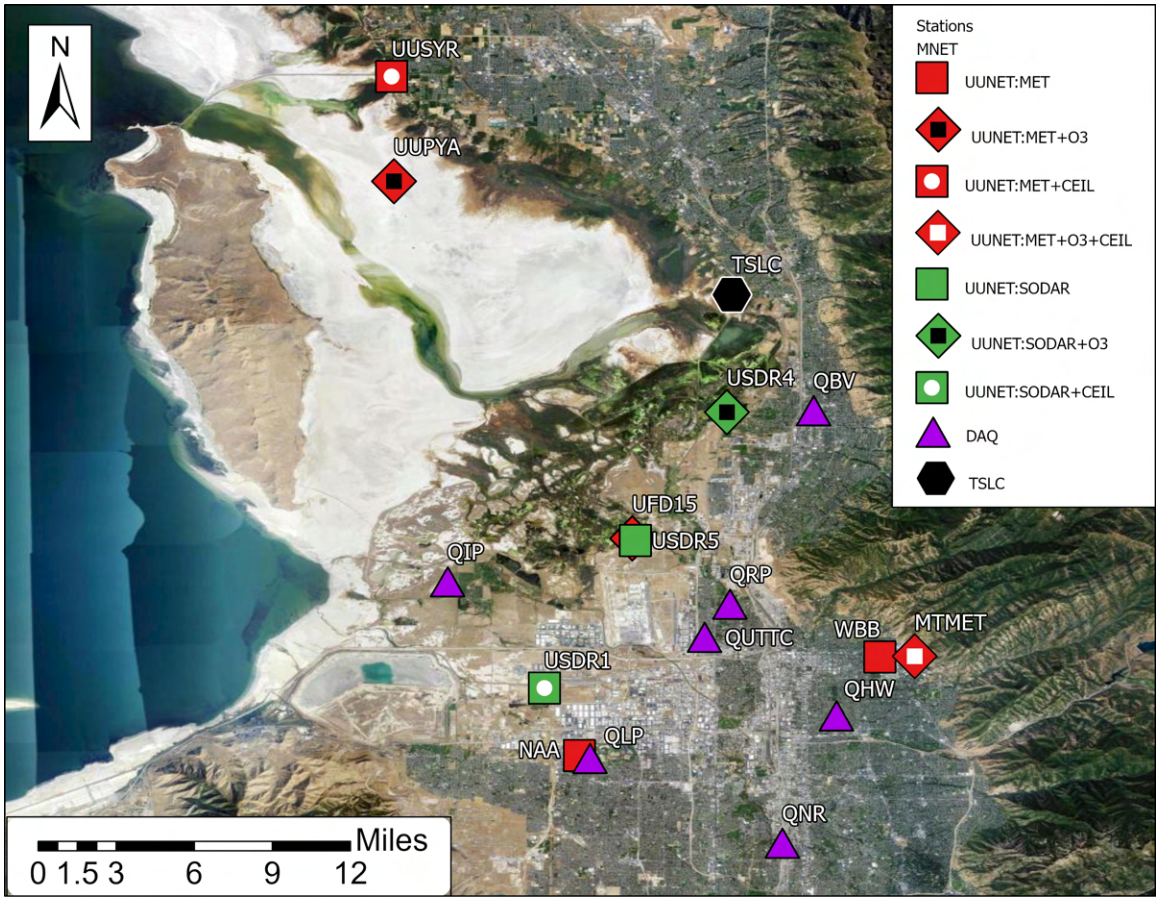

Figure 2.1: Location of key sensors available during the summer 2022 ozone campaign. TSLC is located at the black hexagon. Purple triangles indicate permanent regulatory sensors maintained by DAQ, squares indicate UU equipment sites. Research grade ozone monitors of interest to this study were placed at UUPYA, USDR4, and UFD15. Meteorological sensors were also deployed at UUPYA and UFD15 and sodars at USDR1, USDR4, and USDR5.

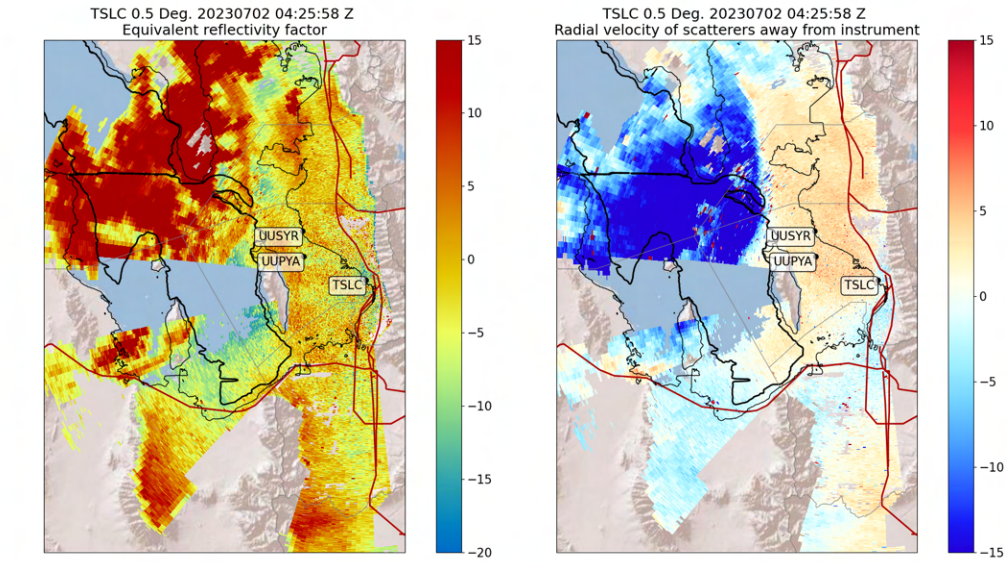

Figure 2.2: Plan view TSLC 0.5° imagery at 0425 UTC 2 Jul 2023. Left figure shows reflectivity (dBZ). Right figure shows radial velocity ($m\ s^{-1}$) with blue indicating motion toward the radar and red indicating motion away according to the scale on the right. Areas on all sides except for northwest lacking data are empty due to beam blockage by topography.

CHAPTER 3

TSLC RADAR RETRIEVAL METHODOLOGY

This study makes use of retrievals from TSLC designed to determine atmospheric state in the vicinity of the radar that are variants on the velocity azimuth display (VAD) and quasi-vertical profile (QVP) retrieval methods. VAD retrievals operate on the Doppler effect and have been used for both radar and lidar radial velocity data with appropriate scanning strategies. Radial velocity reports the component of scatterer motion toward or away from the radar. For a gate at an azimuth relative to north α and elevation angle ϕ, the Cartesian wind components at that location contribute to radial velocity as follows (assuming geometric beam propagation):

$$V_r = u\ sin(\alpha)cos(\phi) + v\ cos(\alpha)cos(\phi) + w\ sin(\phi). \tag{3.1}$$

When scatterers are primarily being moved by the mean wind, as is generally the case under clear air conditions, radial velocity magnitude will be maximized when at an azimuth facing directly into or away from the mean wind, and zero when facing perpendicular. When radial velocity at a constant range and elevation angle is plotted against azimuth in flow uniform over the entire range ring, a sinusoidal pattern appears in the data. The phase and amplitude of this sinusoid can reveal properties about the mean flow. Stacking these rings together and using the beam height at a given elevation angle, a wind profile with respect to height can be determined (Lhermitte and Atlas 1961; Browning and Wexler 1968; Doviak and Zrnic 1993). The QVP makes use of the same range-height relationship, but examines other products and simply takes the mean relying on a uniform scatterer assumption (Ryzhkov et al. 2016). An illustration of the range-height relationship for the clear air volume coverage pattern (VCP) from TSLC is given in Fig. 3.1.

Numerically, mean wind estimation can be done in a number of ways. If observations were perfect, three independent azimuthal samples could be used to solve for the three wind

components. In practice, system noise and turbulence contribute to variance within radial velocity measurements, and treatment of noise becomes necessary for a stable retrieval (Teschke and Lehmann 2017). VADs were initially done using Fourier transforms that require unrealistic uniform sampling around the range ring (Browning and Wexler 1968), so sinusoidal least-squares fit methods are now preferred. The least-squares and Fourier methods converge to the same equations if uniform sampling is assumed (Teschke and Lehmann 2017).

Traditionally VADs are done on one conical scan, but radars usually make more than one conical scan per volume at varying elevation angles, causing the user to select one best suited to their application. High angle scans rely on a smaller area over which uniform flow is assumed, but have lower vertical resolution. On the other hand, low angle scans provide high vertical resolution but the area over which uniform flow is assumed grows rapidly with height and the vertical wind component is not well sampled. Some retrievals use composites of multiple scans to reduce trade offs. NEXRAD level 3 processing and HRRR assimilation use the Extended VAD (EVAD) retrieval (Matejka and Srivastava 1991), which interpolates between the results of individual conical scans onto a common height axis.

This study makes use of the VVP (Waldteufel and Corbin 1979; Boccippio 1995), an alternative that increases the complexity of the regression matrix to accommodate regression over gates with more than one elevation angle. A conceptual model is presented in Fig. 3.2. The VVP partitions gates into constant height disks of some radius above the radar and regresses over all of them at once, more equitably treating noise and increasing regression accuracy. Statistics from the other moments can be gathered from the collections of gates in constant height disks to obtain information about the scatterers, and this retrieval is called an RD-QVP (Tobin and Kumjian 2017). The uniformity assumption still applies in VVPs and RD-QVPs but is unrealistic to apply over the entire sampled volume. As a result, a maximum horizontal distance for valid gates is chosen, creating a cylinder divided into disks of samples to derive the flow field from.

VAD and QVP retrievals done in prior studies with NEXRAD generally use a cylinder radius of 50 km around the radar (Ryzhkov et al. 2016; Griffin et al. 2018; Tobin and Kumjian 2017; Hu and Ryzhkov 2022) or 40 km (Boccippio 1995) to maximize the statistical robustness

of retrieval results. This approach assumes homogeneous flow and scatterers over a large area, an assumption almost never met over such areas in complex terrain (Fig. 3.3). C-Band TSLC scans have shorter gate length than S-Band NEXRAD scans, allowing a greater number of samples to be integrated into the retrieval. However, using a 25 km radius as done for European C-band radars (Holleman 2005) would prove too large for TSLC, located 5 km from the foothills of the Wasatch. Thus, a 5 km radius was used for TSLC, which also reduces the impacts of the commonly-observed Weber Canyon exit jet located to the north (Chrust et al. 2013). The decrease in regressed-over gates is slightly offset by the steeper and more numerous elevation angles of TSLC's clear air VCP compared to NEXRAD's, but still has effects on the retrievals. RD-QVPs are used in this study primarily to assess scatterer quality and relative quantity so the statistical robustness of this retrieval is not as important as for hydrologic and microphysical applications.

The precise meaning of uniform flow for a VVP varies based on the wind model used for the retrieval. When the VVP was first introduced by Waldteufel and Corbin (1979), the wind model regression included the mean and first-order terms of all three Cartesian wind components, creating a 12 term linear equation to carry out least-squares regression. The VVP proves very sensitive to the appropriateness of the wind model for the flow (Boccippio 1995; Shenghui et al. 2014). Too few terms in the retrieval and the model becomes oversimplified, which may cause the uniformity assumption to be violated. Too many terms and the variability present from noise and floating point error may be inappropriately attributed to the flow field, causing the wind field components to be underestimated. Increasing the number of terms also increases the numerical instability of the retrieval. The signal from the first order terms is generally more subtle than the signal from the mean components of the wind. When the number of gates used is increased by either changing scanning strategy or maximum retrieval radius, the low intensity signal from derivative terms becomes distinguishable from the noise, analogous to using a more sensitive microphone to listen for a pin drop.

Artificial wind fields composed of various combinations of first order components and white noise of varying magnitude were used to evaluate the accuracy of the VVP retrieval for the geometry arising from TSLC's clear air VCP and maximum gate distance of 5 km. The

accuracy of the VVP was tested for a variety of wind models, ranging from a 12 component matrix including all first order terms to a 2 component matrix including only the mean horizontal wind component terms. Testing revealed that the error arising from uncalculated and unresolved derivative terms tends to bias the mean vertical wind component much more than the mean horizontal wind components. In these situations, because the vertical wind component became so large, variability was removed from the horizontal components and caused wind speed to be significantly reduced, although direction remained largely unchanged. If all components of the vertical wind were excluded from the matrix and the mean horizontal wind along with their horizontal derivatives were considered under the same conditions, then the horizontal wind speed tended to vary widely based on included elevation angles. This approach becomes inaccurate with wind speed errors greater than the values of the expected wind speed in the modeled flow. At the 5 km radius, regression over only the mean horizontal wind components gave the most consistently correct result for the horizontal wind. When derivative components remained under $O(10^{-2})\ s^{-1}$ and vertical wind speed remained under $O(10^{2})\ m\ s^{-1}$, wind speed was correct within 2 $m\ s^{-1}$ and wind direction was correct within 5°. As a result, the mean horizontal wind components were the only wind components used in the VVP model for this study.

High quality datasets are vital to retrieval accuracy and success. In addition to velocity, TSLC reports reflectivity and spectrum width for each gate. Prior work examining the boundary layer with clear air returns has identified two predominant scatter types: biota (bugs, birds, etc.) and Bragg scattering (Zrnic and Ryzhkov 1998; Bachmann and Zrnić 2007; Heinselman et al. 2009; Banghoff et al. 2018). Other common radar-detectable phenomena around FBP are surface traffic, air traffic, and precipitation, which create outliers that bias the retrieval. To avoid impacts from any such phenomena, all gates with a reflectivity greater than 30 dBZ are rejected.

The CBL is characterized by a region of low yet detectable reflectivity values extending from the surface and deepening throughout the daylight hours (Heinselman et al. 2009; Banghoff et al. 2018). The lowest reflectivity value reported by TSLC, -20 dBZ, is realistic for clear air scatterers, therefore no lower limit was enforced. Because terrain blockage reports a radial velocity of zero and small radial velocity measurements are generally

untrustworthy, all gates with radial velocities below 0.5 $m\ s^{-1}$ are rejected as well. Spectrum width thresholds were evaluated, but did not improve data quality, as spectrum width and reflectivity were found to be well correlated. After the moment filters are applied, an outlier rejection filter is twice applied to the data (Pichugina et al. 2019; Banta et al. 2020).

The final data quality step in the retrieval is to ensure a large enough sample size was used. Prior data quality measures as well as the low reflectivity of clear air scatterers creates gaps in azimuth within the observed volume. The size at which these gaps become unacceptable in a VAD-style retrieval is not well defined, as the samples must be sufficiently orthogonal to capture wind components. Some authors reject a retrieval if the continuous missing area is larger than 60° (Matejka and Srivastava 1991; Boccippio 1995), while the Doppler beam swing (DBS) strategy commonly used in the lidar community calculates VADs from only 4 - 6 azimuths spaced equally around the instrument (Wildmann et al. 2020; Kristianti et al. 2023). VAD retrievals taken over a 30° sector compared well to in-situ sonic anemometer data (Wang et al. 2015), and VVPs were originally thought to be stable over an area as small as 22.5° (Schwiesow et al. 1985). Given these earlier results and the VVPs dependence on a large statistical sample, a disk's retrieval was rejected if less than 15 gates were included in the regression. A final goodness of fit condition was also considered, but required too much tuning to prove useful.

The resulting VVP and RD-QVP data are then available every 6 min at 50 m intervals in the vertical. For clarity in many figures, light smoothing is applied using a five-point stencil (incorporating those values immediately adjacent in time and in the vertical).

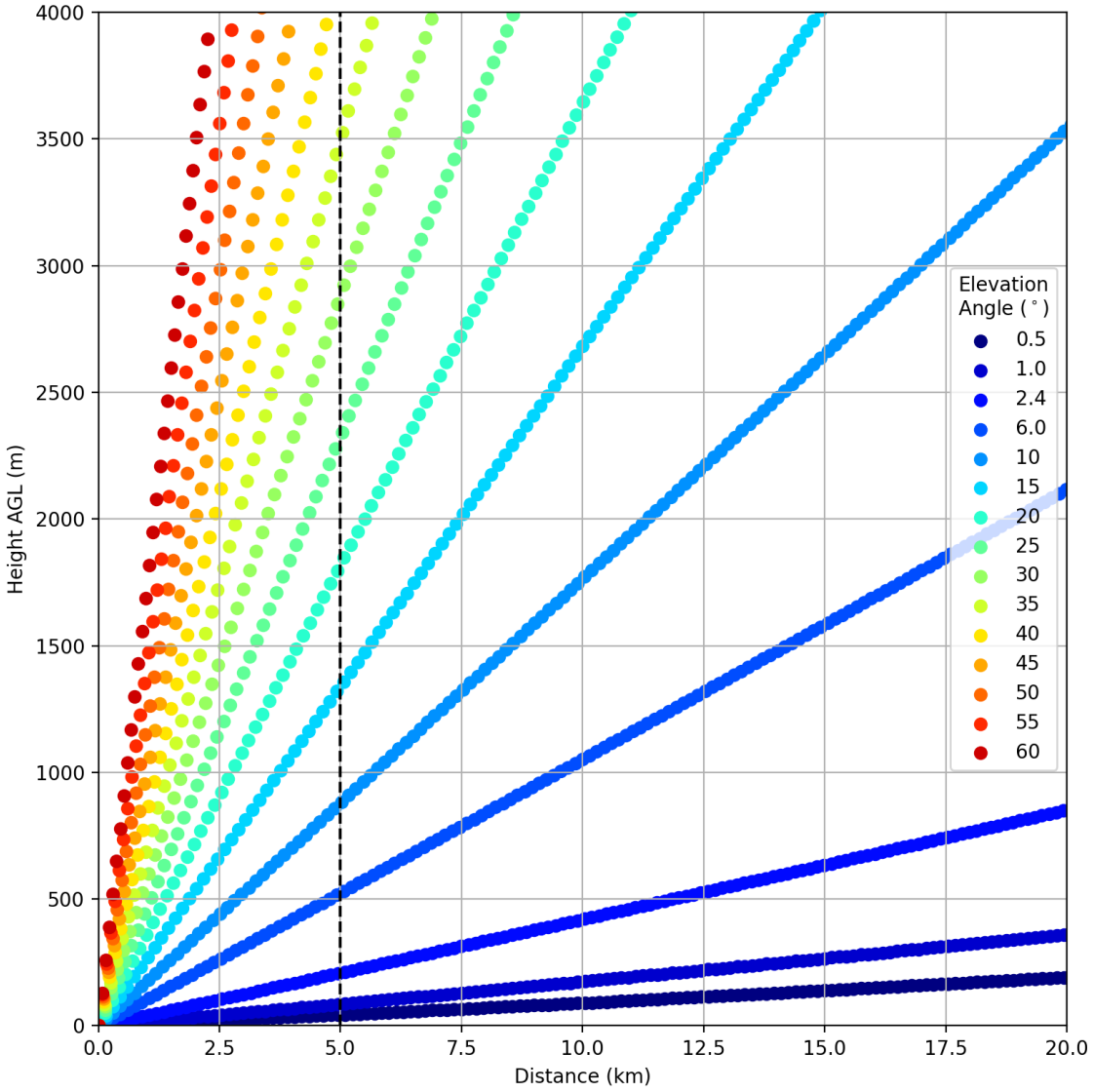

Figure 3.1: TSLC VCP 90. Beam height (m) as a function of gate distance (km) from the radar at an elevation angle is represented by the colored dots. Black dashed line indicates 5 km distance limit used for retrievals in this study. The radar progresses from the lowest elevation angle to the highest during a volume scan.

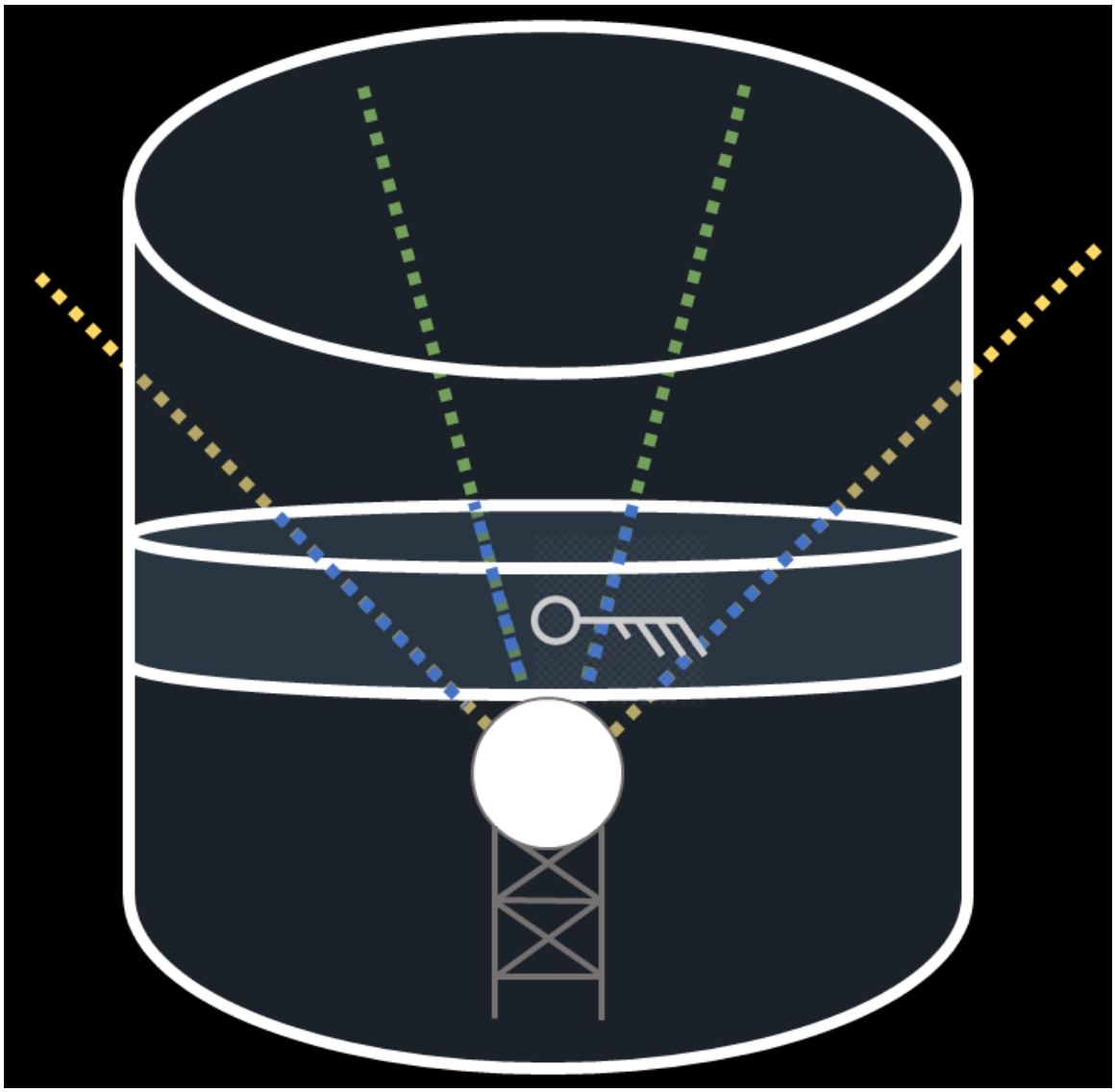

Figure 3.2: Conceptual model of the VVP retrieval.

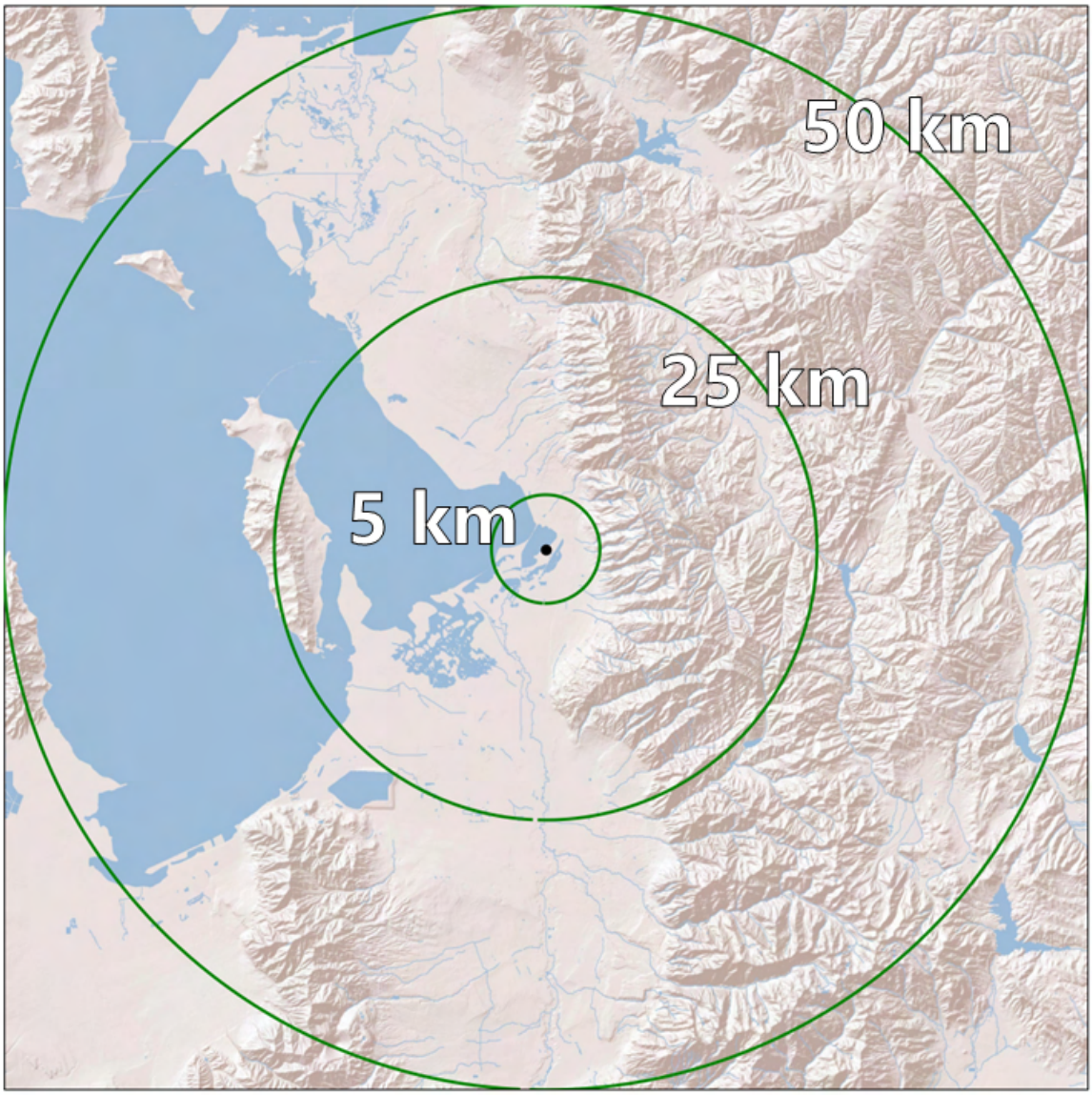

Figure 3.3: A map indicating rings of constant range at 5, 25, and 50 km from TSLC.

CHAPTER 4

LABOR DAY PERIOD (LDP) ANALYSIS

4.1 Overview

The LDP occurred during an abnormally strong late-summer heat wave over the Intermountain West that caused high ozone concentrations in SLV and FBP basins (Fig. 4.1). This period contained a large share of total $\overline{O_3}$ NAAQS exceedances during summer 2022, here defined as 15 Jun - 15 Sep (Horel et al. 2023). The DAQ site in Bountiful, UT (QBV), closest to FBP, exceeded NAAQS a total of 10 times during the summer, with 3 events occurring during the LDP. The DAQ sensor at Hawthorne Elementary in central SLV (QHW) exceeded NAAQS 5 times, with 2 events during the LDP.

The heat wave responsible for this event caused September 2022 to be the warmest recorded September to date in Utah and Nevada, and the second warmest in California, Idaho, Wyoming, and Arizona (NOAA NCEI 2022b). It resulted from a strong ridge in place over the western contiguous United States (Fig. 4.2). The ridge had been present for most of August but located further to the northwest, bringing the warmest August to date in Idaho, Oregon, and Washington state (NOAA NCEI 2022a). Northern Utah was on the perimeter of this system, thus was frequently ventilated by upper-level weather disturbances that reduced pollutant concentrations in the urban boundary layer through vertical mixing and horizontal transport. Prior to the LDP, ozone concentrations during August built in response to increasing stability aloft during periods lasting a few days, having one or two NAAQS exceedance or near-exceedance events followed by a disturbance, after which the cycle would start anew. The cycle of interest here developed after a weak disturbance crossed northwestern Utah on 28 Aug and ended on 8 Sep with the passage of the remnants of Tropical Cyclone Kay. Record high temperatures and high ozone continued 9-12 Sep, but those days were influenced by regional transport of wildfire smoke.

Synoptic conditions during the LDP were quite similar between each day and matched what is often observed during other quiescent periods. Every day except for 30 Aug and 1 Sep lacked significant cloud cover in the basin according to shortwave radiation intensity observed at UUPYA (not shown). Surface observations and near surface conditions available from routinely launched radiosondes from KSLC were generally what is commonly expected during weakly-forced situations. For example, the morning sounding on 5 Sep (Fig. 4.3a) contains a surface-based inversion to a depth of 825 hPa that formed in response to radiative cooling under clear skies. This was topped by a nearly dry adiabatic layer up to 550 hPa, which has its origins in the deep turbulent mixing of the previous day. Weak winds are present through the depth of the profile. The following late afternoon sounding (Fig. 4.3b) shows that this stable layer was eroded and replaced by a shallow surface superadiabatic layer, and afternoon turbulent mixing deepened the mixed layer to 500 hPa. Vertical momentum transport throughout this adiabatic layer likely contributed to the deep northwesterly winds evident in Fig. 4.3b.

A time-height section of vertical potential temperature gradient from the surface to 4000 m AGL was derived from hourly HRRR analysis gridpoint values near TSLC during the LDP. (Fig. 4.4a). Strong stability develops near the surface overnight that significantly weakens during the day. Within HRRR analysis wind speeds at the same location to 2000 m AGL (Fig. 4.4b), slow wind speeds are present in the morning stable layer, increasing in intensity after sunrise with nearly uniform, faster wind speeds evident throughout the column during the afternoon

For reference and comparison to the HRRR wind speed time-height section during the LDP, the time-height section of TSLC VVP wind speed is shown in Fig. 4.4c. The general patterns between the HRRR and TSLC profiles are similar with weaker winds at night and strong winds throughout the lowest 2 km during the afternoons. However, some weak horizontal banded artifacts appear in the VVP retrievals at 100 m, 200 m, 500 m, 800 m, 1300 m, 1800 m, and 1900 m. These are a result of gates for particular elevation angles being dropped from the retrieval. They are believed to occur because of unresolvable derivative terms in the wind model. Errors from unresolved derivatives are more problematic at low wind speeds, which are common within the LDP's nighttime residual layer.

Hourly HRRR 80 m winds for northern Utah during the LDP show local thermally driven circulations dominating the flow pattern near the surface. In the morning hours (e.g., Fig. 4.5a) southerly flow is present through the length of the SLV with easterly winds to the north of Antelope Island. There is also an area of confluence in the southwest corner of the GSL. The southerly flow near the Wasatch Mountains becomes southeasterly, indicating influence from the model's limited resolution of local downslope flows. During the afternoon (Fig. 4.5b), this flow reverses and becomes faster and northerly over FBP and the SLV with a diffluent zone on the northwest side of the GSL.

A composite figure of key datasets for the LDP is presented in Fig. 4.6. We begin this discussion by considering O_3 (Fig. 4.6a) and ozone time rates of change (O_3') (Fig. 4.6b) computed for seven sites. Composites for the DAQ sites were created by averaging the hourly observations across all days. Composites for UU sites were created using the one-hour average for the same hour as the DAQ observations. $O_3'$was calculated from the hourly data for DAQ sites and one-hour average smoothed data for UU sites then had the same averaging applied to create the composite presented here.

Beginning with the composite average derived from the mean of all seven sites (black solid line in these figures), common features are evident:

- O_3 is lowest near sunrise (0600-0700 MDT) and then rises sharply with increases of roughly 5-12 $ppb\ h^{-1}$until after solar noon (1300 MDT);
- O_3 decreases slowly after that time due to mixing within the CBL until sunset (1900-2000 MDT) after which O_3 decreases faster until after midnight.
- Between midnight and sunrise, O_3 tends to stay mostly constant.

During the overnight hours the individual time series of O_3 tends to fall within a low or high cluster around the composite mean, with urban sites (QBV, QHW) above the mean and FBP sites (USDR4, UFD15, UUPYA) below the mean. Ozone at the latter sites increases rapidly, with O_3' peaking earlier in the day than the former. DAQ sites QIP and QRP on average exhibit a mix of these two signals, reflecting their siting closer to Gilbert Bay and northern SLV urban area, respectively. UFD15 tends to have higher than average O_3 during the morning increase and has the greatest daily swing of all sites, while UUPYA and USDR4 consistently have O_3 lower than other sites.

Composite VVP winds for the LDP period are shown in Fig. 4.6c. VVPs were averaged in height along the native axis and time bins of 18 minutes, corresponding to roughly 3 volume scans. For all 50 m constant-height increments, zonal (u) and meridional (v) wind components were averaged separately from the composite wind speed. The composite direction was derived from the mean u and v components. Several key typical features during the LDP are as follows:

- Weak winds aloft in the 250-1250 m layer prior to sunrise transition to weak easterly flow after 0700 MDT;
- Northeasterly-easterly winds below 250 m develop after 0800 MDT and then veer abruptly with time to westerly winds between 1000 and 1100 MDT;
- As the near-surface winds become westerly, the winds below 1000m become southerly;
- As the stable boundary layer weakens during the late morning and the CBL develops, this wind shear layer lifts rapidly by 1200 MDT to 1000m;
- By solar noon (1300 MDT), the CBL has deepened to higher than 2000m and the winds after that time are the strongest of the day from the northwest until sunset.

Reflectivity RD-QVPs were composited in the same manner as composite wind speed and shown in Fig. 4.6d. Sun glint from sunrise and sunset are indicated by smoothed spikes below 500 m of surface based reflectivity near 0630 MDT and 2000 MDT. As the surface inversion erodes after 0800 MDT, reflectivity begins to increase synchronously with the development of vertical wind shear aloft that indicates the development of a shallow CBL. Scatterers are mixed vertically through the lowest 500 m by 1030 MDT while the highest near-surface reflectivity (7 dBZ) occurs near 1100 MDT. After this time, horizontal and vertical turbulent mixing reduces reflectivity as the CBL continues to expand above 2000 m by 1400 MDT. The ceilometers deployed for the 2022 field program (Horel et al. 2023) used for boundary layer depth estimation returned aerosol backscatter signatures similar to what is seen in the RD-QVP (not shown). Before sunset, a plume of higher reflectivity is apparent 1900 - 2030 MDT with a maximum depth of 1000 m, corresponding to bird activity near the radar.

The composite panels in Fig. 4.6 help to delineate core features in ozone concentrations and wind that are commonly found during all ten days of the LDP. However, the day-to-day

variations in mesoscale circulations and local thermally-driven flows introduce differences in the boundary layer structure, particularly during the morning when ozone concentrations are rapidly increasing. These differences are explored in the following subsection.

4.2 Individual Days

During the late afternoon when the CBL is fully developed and after sunset, ozone concentrations and vertical wind profiles within the region of interest during the LDP tended to evolve similarly (Fig. 4.6): late-afternoon concentrations dropped slowly co-occuring with strong northwesterly winds until after sunset. However, conditions differ day-to-day from sunrise until the CBL is fully formed and are the focus of this sub-section. Hourly DAQ data and one-hour running mean smoothed UU data for O_3 are presented in subfigure (a) of each figure. The black mean line was calculated using the hourly DAQ values and the UU observations from the same hour. O_3'(subfigure b) for each station was calculated as the time rate of change in $ppb\ h^{-1}$and the mean line calculated in the same manner as that for O_3. VVPs (subfigure c) and RD-QVPs (subfigure d) are presented in full resolution of 50 m in the vertical and 1 volume (roughly 6 minutes) in time. Every third barb in time is plotted on the figure.

4.2.1 29 August

Overall, the evolution of ozone, wind, and reflectivity during 29 Aug (Fig. 4.7) followed the core composite signals. This day was cooler (Fig. 4.1b) than later days without any $\overline{O_3}$ exceedances at the seven sites (Fig. 4.1a). QBV in Davis County reached higher O_3 concentrations than nearly all other sites by 1100 MDT with an hourly increase of 20 ppb during the previous hour. In the SLV, QRP and QHW reached the highest O_3 at 1400 MDT and 1500 MDT, respectively preceded by 20 ppb increases during those previous hours (Fig. 4.7a).

Easterly flow was present on 29 Aug in a shallow near-surface layer beginning at 0830 MDT that grew to roughly 300 m by 1000 MDT with increased reflectivity within this layer (Fig. 4.7c, d). Perhaps independently, higher reflectivity associated with easterly winds is evident within the RL between 400-500 m until 1100 MDT. As the stable layer

continues to erode during mid-morning, the near-surface easterly winds shift to northerly and then westerly abruptly at 1100 MDT. The shear line rapidly lifts to 600 m by 1200 MDT at which time reflectivity begins to drop. The shear layer moves to 1300 m by 1400 MDT, and progresses to the top of the profile by 1600 MDT.

4.2.2 30 August

Multiple wind shifts occurred near the surface during the morning of 30 Aug (Fig. 4.8c), which was a cooler day with only one $\overline{O_3}$ exceedance at QIP (Fig. 4.1). After sunrise, northerly winds below 250 m shifted to easterly by 0900 MDT that later shifted again from northeasterly to northwesterly by 1030 MDT. The CBL was likely 500 m during this period and that northwesterly flow persisted until roughly 1300 MDT. A separate wind shift from easterly to westerly developed in the 500-800 m layer at 1230 MDT. By this time, the large and positive O_3' previously at UFD15, USDR4, and UUPYA began decreasing, likely resulting from the deepening CBL. By 1400 MDT, these distinct wind layers merged into the typical deep afternoon northwesterly flow leading to peak ozone at QIP and QRP at this time followed by large O_3' at those locations during the next hour(Fig. 4.8). Despite that initial sudden dropoff in O_3, QIP remained higher than the other stations until 1700 MDT.

4.2.3 31 August

The time-height profile for 31 Aug shows fairly typical boundary layer development, with the morning flow reversal happening at 1000 MDT to a depth of 250 m. The shear layer then moves from 250 to 900 m in a fairly linear fashion 1000-1200 MDT, suddenly increasing to 1300 m at 1200 MDT. After this time, the shear layer apppears as a subtle shift from northeasterly flow to northwesterly flow in the layer above 1300 m by 1500 MDT, after which flow becomes consistently northwesterly through the depth of the profile. The center stations stretching southward from FBP into the SLV (e.g., UFD15, QRP, and QHW) reported high peak ozone at 1400 MDT and then decreased rapidly through the late afternoon hours (Fig. 4.9b).

QIP was again the only one of the seven stations to report an exceedance event on 31 Aug (Fig. 4.1) and O_3 tended to be higher than that at other stations throughout the day

(Fig. 4.9a). The time-height profiles near the TSLC are less informative for explaining the O_3 exceedances on 30-31 Aug at QIP. While QIP is the closest of the seven stations to Gilbert Bay and typically influenced by lake breezes penetrating southwest into the SLV, weak lake breezes on 30-31 Aug were limited to the far western SLV. A Utah Department of Transportation station located 7 km southwest of QIP recorded the lake breeze passage at 1030 MDT on 31 Aug (not shown). However, QIP experienced easterly winds until after 1600 MDT and never exhibited an increase in dew point temperature and slight drop in temperature typically observed with the passage of a lake breeze (not shown). Blaylock et al. (2017) examined the propagation down the SLV of a strong lake breeze front with high O_3 concentrations in the confluence zone immediately behind the leading edge of the front. In contrast, Banta et al. (2011) highlighted that ozone concentrations can be enhanced by flow convergence ahead of sea-breeze fronts that often stall near coastlines. Stalling of the lake breeze is thought to be responsible for QIP's high ozone concentrations on 30 and 31 Aug.

Plan view 0.5° reflectivity and radial velocity images from TSLC on 31 Aug are shown in Fig. 4.10 to illustrate how the complex flows in the region tended to keep QIP downstream of flow from the urban corridor to its east sandwiched between nearby lake and playa breezes. The onshore lake breeze began to be evident near 1030 MDT (Fig. 4.10a) in the gap between the Oquirrh Mountains and Antelope Island, just to the west of QIP. Southerly flow dominates the SLV at this time. The weak lake-breeze feature is marked by a region of outbound winds (red) near QIP and decreased inbound winds (blue) further to its south. Simultaneously, a wetland/playa breeze began developing in the FBP with winds approximately normal to radar beam propagation, thus is more evident in reflectivity by an area of increased, narrowing bands of reflectivity over time stretching roughly from TSLC to the southern tip of Antelope Island that intensified through the morning hours.

By 1200 MDT (Fig. 4.10b), the southerly flow through SLV weakened, allowing the lake breeze to begin propagating southeast adjacent to the Oquirrh Mountains yet not crossing QIP. The confluence zone associated with the playa breeze between TSLC and QIP is quite apparent from the pairing of high reflectivities and low, variable radial velocities from biota. The lake breeze progressed southward and weakened as it penetrated into the SLV (Fig.

4.10c). During this same period, the playa breeze began developing a weak reflectivity band at its leading edge extending eastward from Antelope Island with QIP still to the south of the intersection. The playa breeze remains evident in the reflectivity band extending southeastward from Antelope Island yet remains north of QIP at that time (Fig. 4.10d) and stalls north of QIP throughout the rest of the afternoon (Fig. 4.10e).

4.2.4 1 September

O_3 remained lower than other LDP days during 1 Sep, with stations in Davis County (UFD15 and QBV) reporting the overall highest concentrations during 1300-1500 MDT (Fig. 4.11a, b). After a brief burst of southerly winds at sunrise on 1 Sep, the winds below 250 m rotated from northwesterly to easterly from 0700-1000 MDT (Fig. 4.11c). This was followed by a short period of shallow northerly wind below 250 m and southerly winds above that until 1130 MDT when deeper southwesterly winds began to develop. Northwesterly winds then became evident throughout the column by 1400 MDT. As seen in other early mornings, higher reflectivity values appear to be present in the RL at times between 9 and 1100 MDT (Fig. 4.11d).

4.2.5 2 September

Lower O_3' during the morning of 2 Sep suggests that production was less efficient than that during other days (Fig. 4.12), leading to maximum O_3 values of roughly 70 ppb. A shallow surface-based layer of easterly flow develops at 0800 MDT that deepens and becomes northwesterly by 1000 MDT. Easterly flow is present aloft above that shallow layer to 800 m. The near-surface flow reversal happens shortly before 1100 MDT and the shear zone increases to a height of 500 m, and not increasing again until 1300 MDT at which point the flow became northwesterly through the depth of the profile, which is earlier than during previous days. O_3 remains nearly constant during the afternoon without the sharp peaks and falls observed during other afternoons previously. Hence, the dilution effect from vertical mixing of lower background O_3 concentrations aloft with higher near-surface concentrations was less evident.

4.2.6 3 September

Elevated O_3 concentrations were especially pronounced during the morning hours of 3 Sep at QRP in the northern end of the SLV's urban corridor (Fig. 4.13a, b). Many sites had O_3' greater than 20 $ppb\ h^{-1}$ at times during the morning with sharp decreases at UFD15, QBV, and USDR4 between 1500-1600 MDT. A weak shortwave trough propagated through northern Utah during the day 3 Sep that primarily affected the flow above the boundary layer, leading to a distinct layer between 500-1250 m of southerly flow preceding the trough passage at 1400 MDT (Fig. 4.13c). Northerly flow developed after sunrise below 250 m with easterly flow between 250-500 m. While the shear layer remained at roughly 250 m until 1300 MDT, the flow after 1100 MDT transitioned to northwesterly below and southerly above this shear layer that then increased in depth to 800 m by 1400 MDT. The shallow boundary layer until 1300 MDT may have contributed to the rapid increases in O_3 prior to solar noon.

4.2.7 4 September

$\overline{O_3}$ concentrations at QBV and UFD15 stood out on 4 Sep, having much greater $\overline{O_3}$ than other stations on this day (Fig. 4.13a). O_3 itself was elevated at stations on the eastern portion of the study area, with QBV above the 7-station average during almost the entire day by as large as 25 ppb, and UFD15 above the average by as much as 20 ppb during 1100-1500 MDT. USDR4 and UUPYA, which typically exhibit lower ozone concentrations than other field sites, were near the average during 0900-1400 MDT. The near-surface shear layer in the VVP became apparent at 0730 MDT and grew to a depth of 400 m by 0830 MDT and gradually lowering to 250 m through the morning hours (Fig. 4.14c). Southerly flow dominated above that layer without the more typical easterly flow aloft during this period. Near-surface flow reversal occurred later than usual at 1100 MDT, switching from northerly flow to southwesterly reflecting flow from the SLV urban area continuing into the wetland regions of the FBP. Westerly flow then dominates from the surface through 800 m until sunset through most of the layer.

The predominant westerly flow during the afternoon was likely a contributor to high ozone concentrations in the eastern part of the study domain. Advection can be an im-

portant process for reducing ozone concentrations (Banta et al. 2011), but in regions of complex terrain like northern Utah, wind can be more or less efficient at transporting ozone depending on its relationship with terrain barriers. Near FBP, the most significant terrain barrier is the Wasatch mountains on the eastern side of the domain. When flow is westerly, the Wasatch acts as a barrier to that flow, and ozone must be transported either around or over the mountains. Overall, this may lead to less efficient transport of high ozone concentrations for this region than the predominant northwesterly flow present during most of the other afternoons.

4.2.8 5 and 6 September

Lower $\overline{O_3}$ yet higher temperatures transpired during 5 and 6 Sep (Fig. 4.1). The morning and afternoon vertical temperature profiles from the SLC rawinsonde observations shown in Fig. 4.3 highlight the 500 m depth of the strong surface inversion with weak easterly winds immediately above the inversion in the morning that transitions to the deep afternoon CBL with flow from the northwest. The SLC sounding on 6 Sep highlighted stronger winds at 0530 MDT with 10 $m\ s^{-1}$ winds from the north near the surface and from the east at 800 m (not shown). The afternoon sounding on 6 Sep is close to a repeat of that during the previous day (not shown).

QIP and QHW had peak O_3 concentrations on 5 Sep at 1300 MDT and 1400 MDT, respectively, with rapid increases followed by rapid decreases centered at those times (Fig. 4.15a, b). Peak O_3 concentrations occurred later at 1500 MDT on 6 Sep (Fig. 4.16a, b). During both mornings (Figs. 4.15c and 4.16c), persistent and deep easterly flow in the layer above the near surface shear layer is evident. East-northeasterly flow aloft also redeveloped both evenings after sunset. On 5 Sep (Fig. 4.15), the surface shear layer first appears at 0700 MDT at 150 m, staying fairly static until the near-surface flow reversal at 1000 MDT, after which it lifts to 850 m. Between 1030-1200 MDT the layer remains static, again increasing rapidly at 1230 MDT until the CBL extends upwards above 2000 m near 1400 MDT. Near the surface, a layer of southeasterly flow develops after sunrise and deepens to 200 m by 0900 MDT. Weak flow is sandwiched between the easterly winds in the near-surface layer and above 500 m. Near-surface winds transition clockwise from southeast to southwest

between 1000-1100 MDT, instead of from northeast to northwest as occurred during prior days. Flow near the surface becomes westerly by 1230 MDT.

After 0800 MDT on 6 Sep easterly winds extend from the surface to 1300 m that are interrupted in the lowest 800 m by a shift to northerly winds after 1000 MDT followed later by a shift after 1100 MDT to more westerly winds below 500 m. The easterly wind collapse aloft after 1200 MDT but then redevelop after sunset that evening and continue to after 0400 MDT 7 Sep (see Fig. 4.17c). The easterly flow established during the early mornings and after sunset are associated with downslope flows over the Wasatch mountains upstream of FBP and SLV. Lower background O_3 concentrations aloft are hence entrained near or close to the surface and likely contribute to the lower concentrations observed at the seven sites during the rest of the day.

4.2.9 7 September

The final day of the LDP, 7 Sep, had the highest $\overline{O_3}$ concentrations of the period at all of the sites. Only UUPYA remained below near-exceedance concentrations. O_3 peaked at most sites between 1400-1500 MDT with a secondary maxima at QHW at 1800 MDT. O_3 at QBV was higher than all of the other sites through most of the day and was 10-15 ppb higher than other locations. As mentioned earlier, the downslope easterly and southeasterly flow aloft present during the previous two days collapsed after 0400 MDT 7 Sep (Fig. 4.17c). The initial near-surface shear layer between 0400-0600 MDT is consistent with the surface inversion depth of roughly 250 m evident from the SLC radiosonde (not shown). Light near-surface winds developed after sunrise that developed into easterly winds after 0830 MDT. Southerly winds then became established after 1000 MDT that would potentially transport precursor chemicals from urban regions to the south through much of the period until 1400 MDT. Westerly and northwesterly flow in the CBL then becomes established until near sunset. A reflectivity feature evident around 9 AM on several days is evident on 7 Sep (Fig. 4.17d). Reflectivity near the shear layer is lower than reflectivity in regions above and below. Banghoff et al. (2018) illustrated this feature in more detail with QVPs of polarimetric variables.

The LDP was selected for more detailed analysis compared to other periods during the 2022 field study because of the high ozone concentrations during many days. The VVP and RD-QVP retrievals during the LDP had a mix of features commonly observed each day yet had obvious, and important, differences from day-to-day as well. The largest differences arise as a result of the multiple ways that surface inversions near TSLC transition to CBLs and how that information helps inform assessing the timing for peak ozone concentrations in the region.

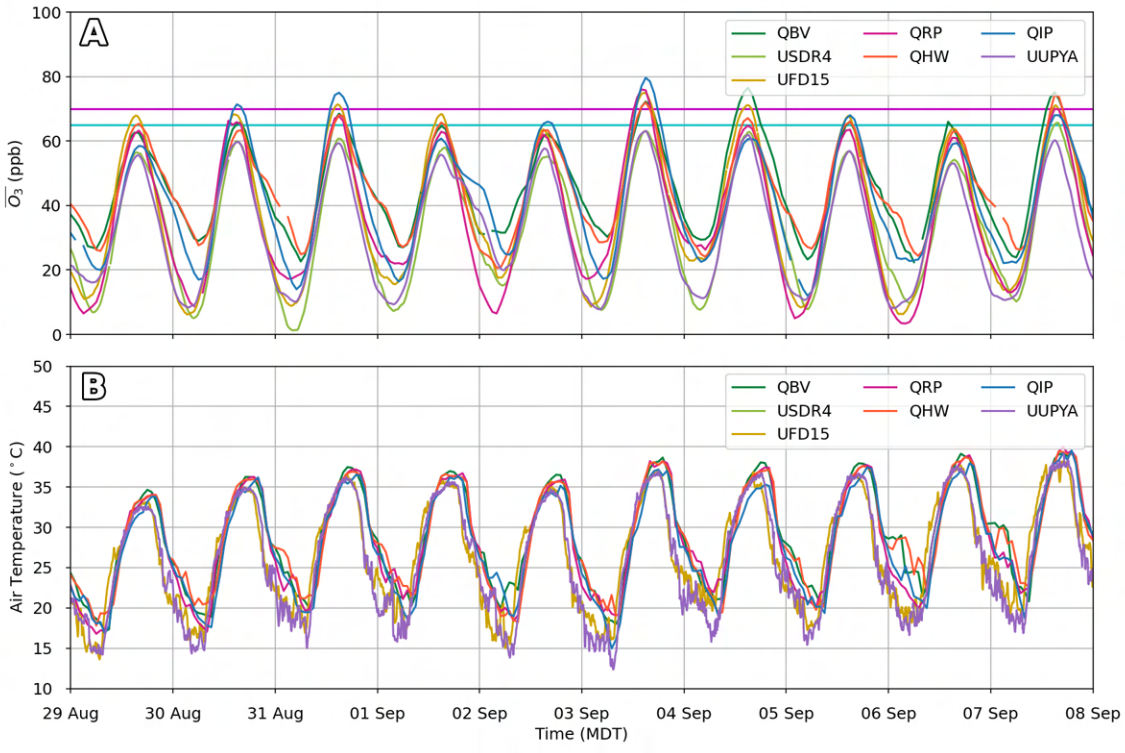

Figure 4.1: Surface station observations from study sites during the LDP. (a) Timeseries of $\overline{O_3}$ (ppb). $\overline{O_3}$ values are computed from hourly (5 min) observations at DAQ (UU) sites, respectively. (b) As in (a) except for air temperature (°C) at hourly (5 min) intervals at DAQ (UU) sites, respectively.

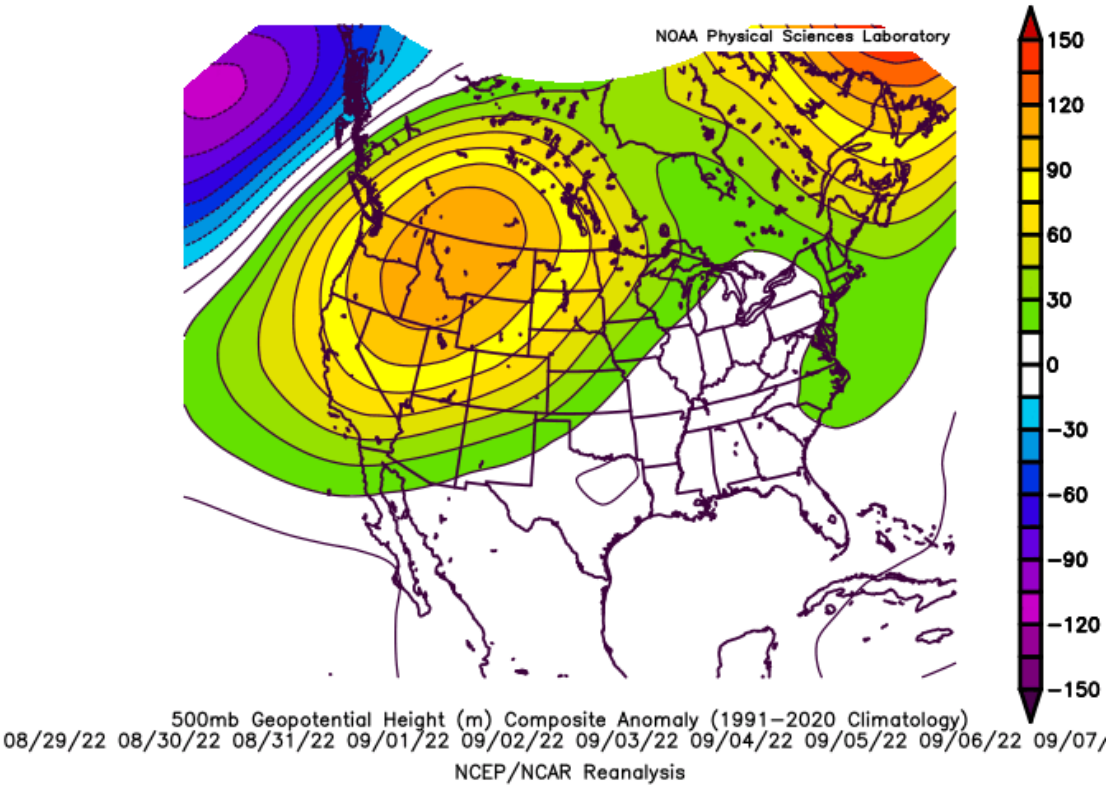

Figure 4.2: NCEP/NCAR reanalysis 500 hPa geopotential height composite anomalies (m) during the Labor Day period relative to the 1991-2020 mean heights.

(a)

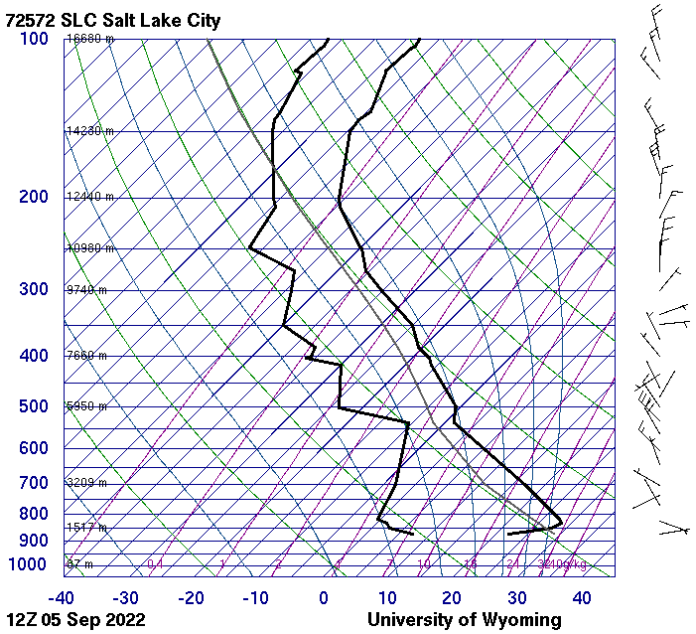

(b)

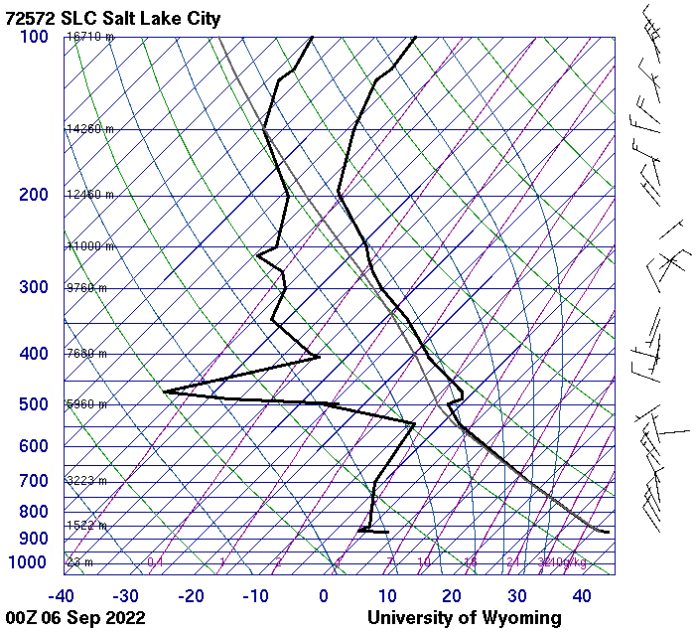

Figure 4.3: Vertical soundings from KSLC. (a) Sounding observed 1200 UTC 5 Sep 2022. (b) As in (a) except at 0000 UTC 6 Sep 2022.

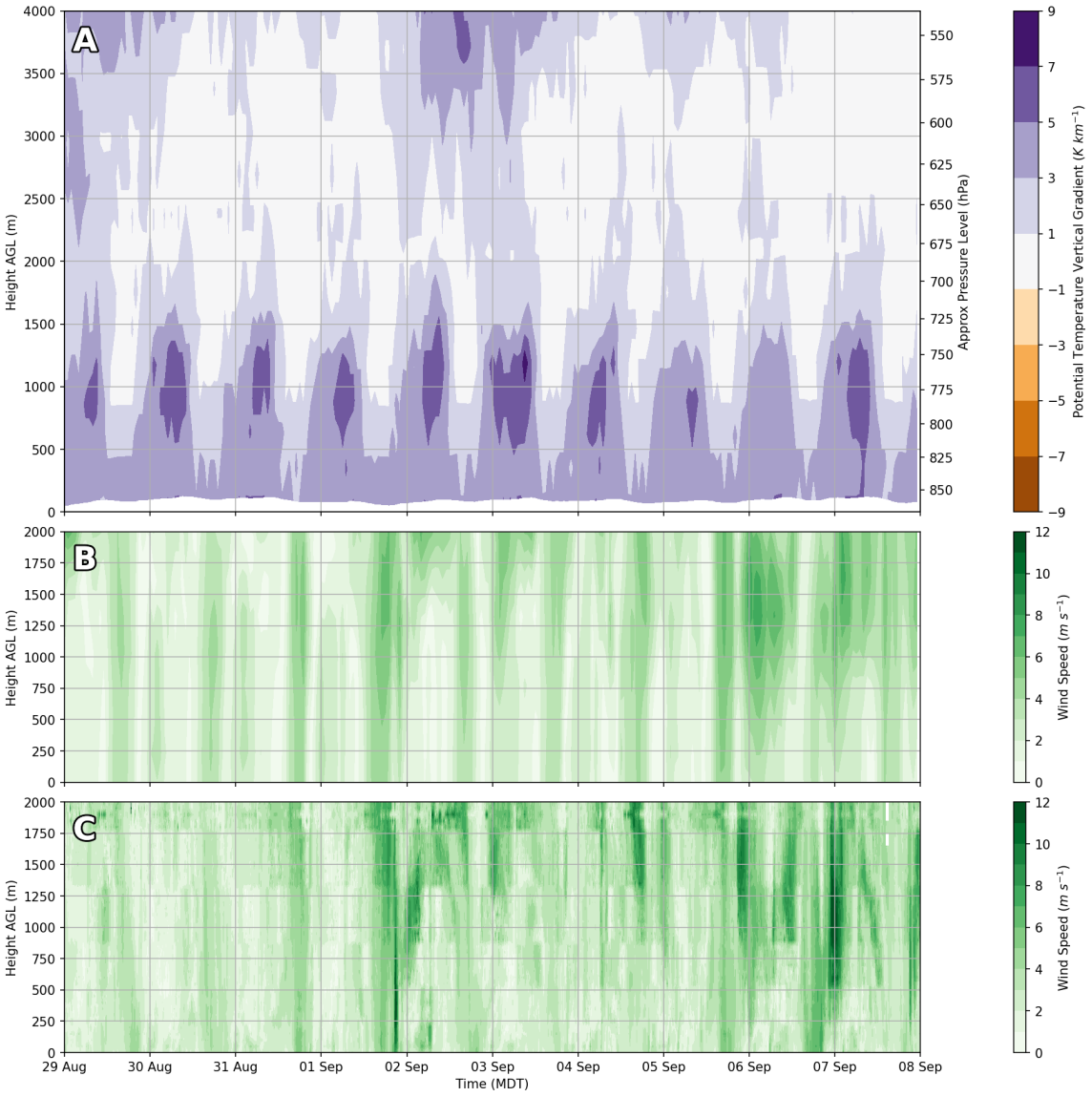

Figure 4.4: Time-height sections from HRRR analysis at 25 hPa intervals in the vertical and VVP wind speeds during the LDP. (a) Time-height sections for HRRR hourly analyses of vertical potential temperature gradient ($K\ km^{-1}$). (b) As in (a) except for HRRR hourly analyses of wind speed ($m\ s^{-1}$). (c) As in (b) except for VVP wind speeds every 6 min during the same period and at 50 m intervals in the vertical.

(a)

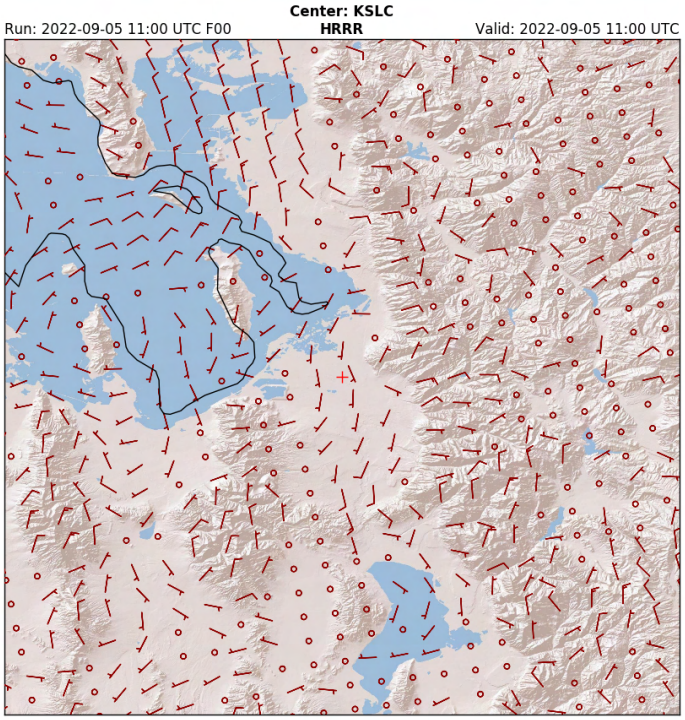

(b)

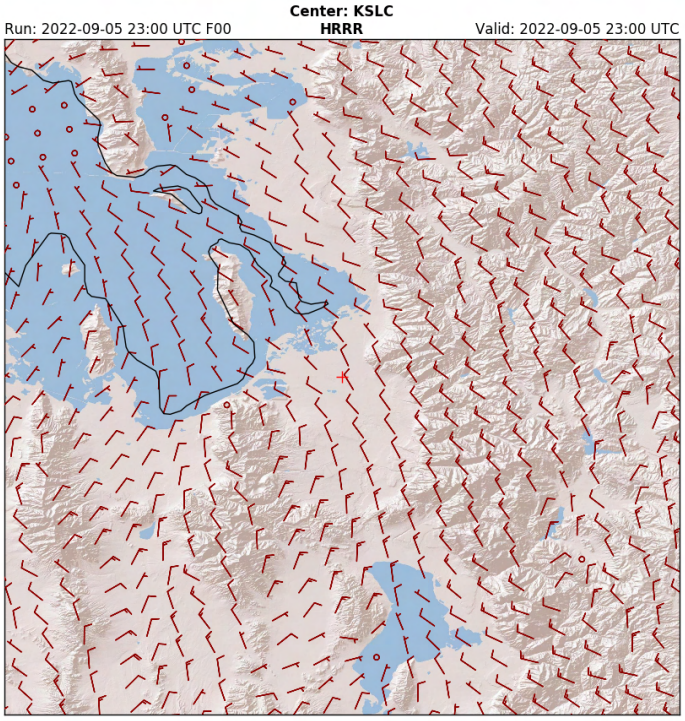

Figure 4.5: HRRR analysis 80 m winds for northern Utah. (a) HRRR analysis valid at 1100 UTC 5 Sep 2022. A half (full) barb corresponds to 2.5 $m\ s^{-1}$ (5 $m\ s^{-1}$) flow. Red cross indicates location of KSLC. Current extent of the Great Salt Lake is outlined in black. (b) As in (a) except at 2300 UTC 5 Sep 2022.

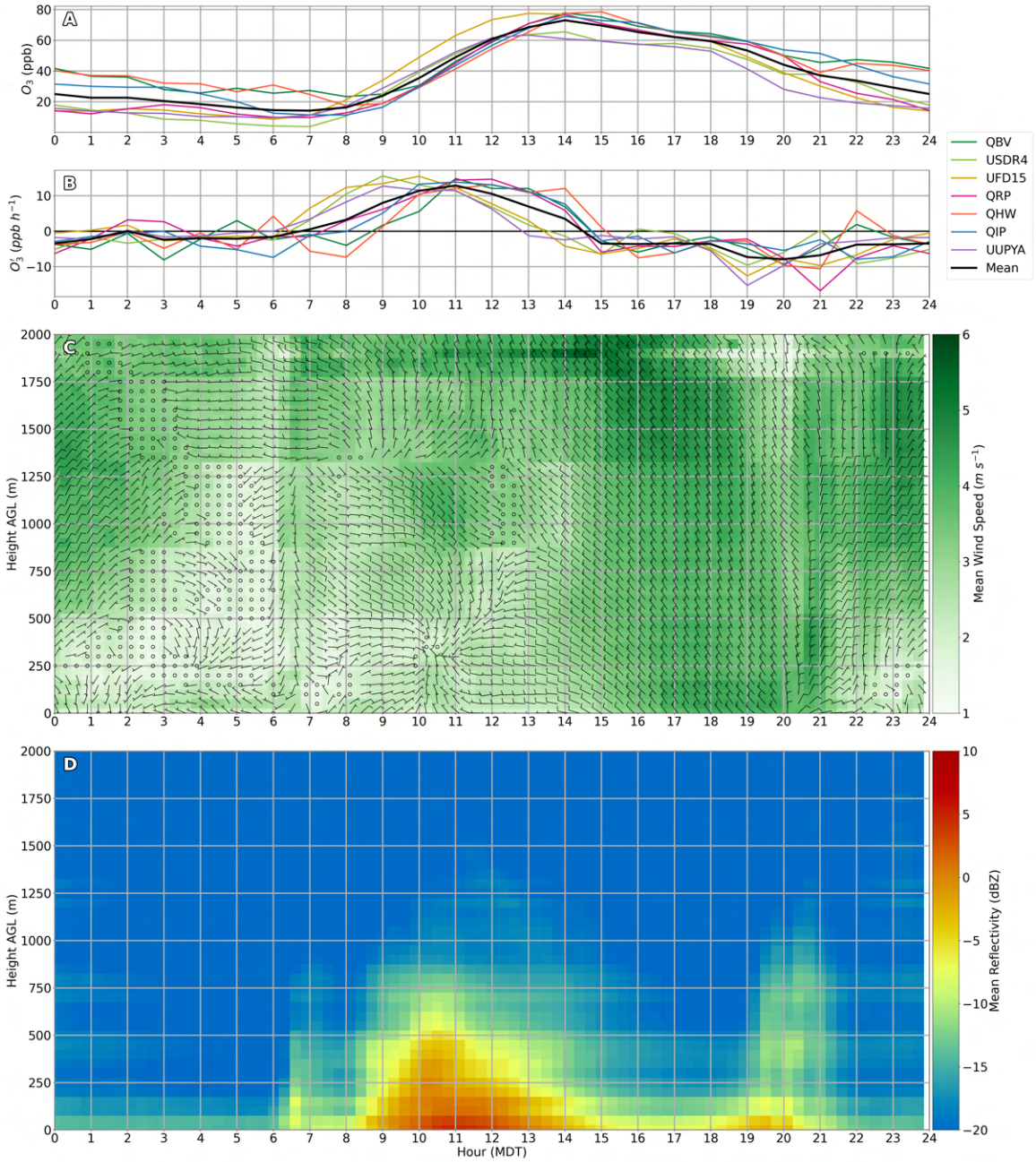

Figure 4.6: Composite of observations made during the ten-day LDP. (a) Composite O_3 (ppb) computed within the LDP of DAQ observations during each hour and hourly running mean observations at UU sites. (b) As in (a) except for O_3' (c) Composite TSLC VVP computed at 50 m intervals in the vertical and every 6 min of the day for wind speed (shaded, $m\ s^{-1}$) and wind barbs during the LDP. Half (full) barbs correspond to 1.25 (2.5) $m\ s^{-1}$. (d) As in (c) except for composite TSLC mean reflectivity RD-QVP (dBZ).

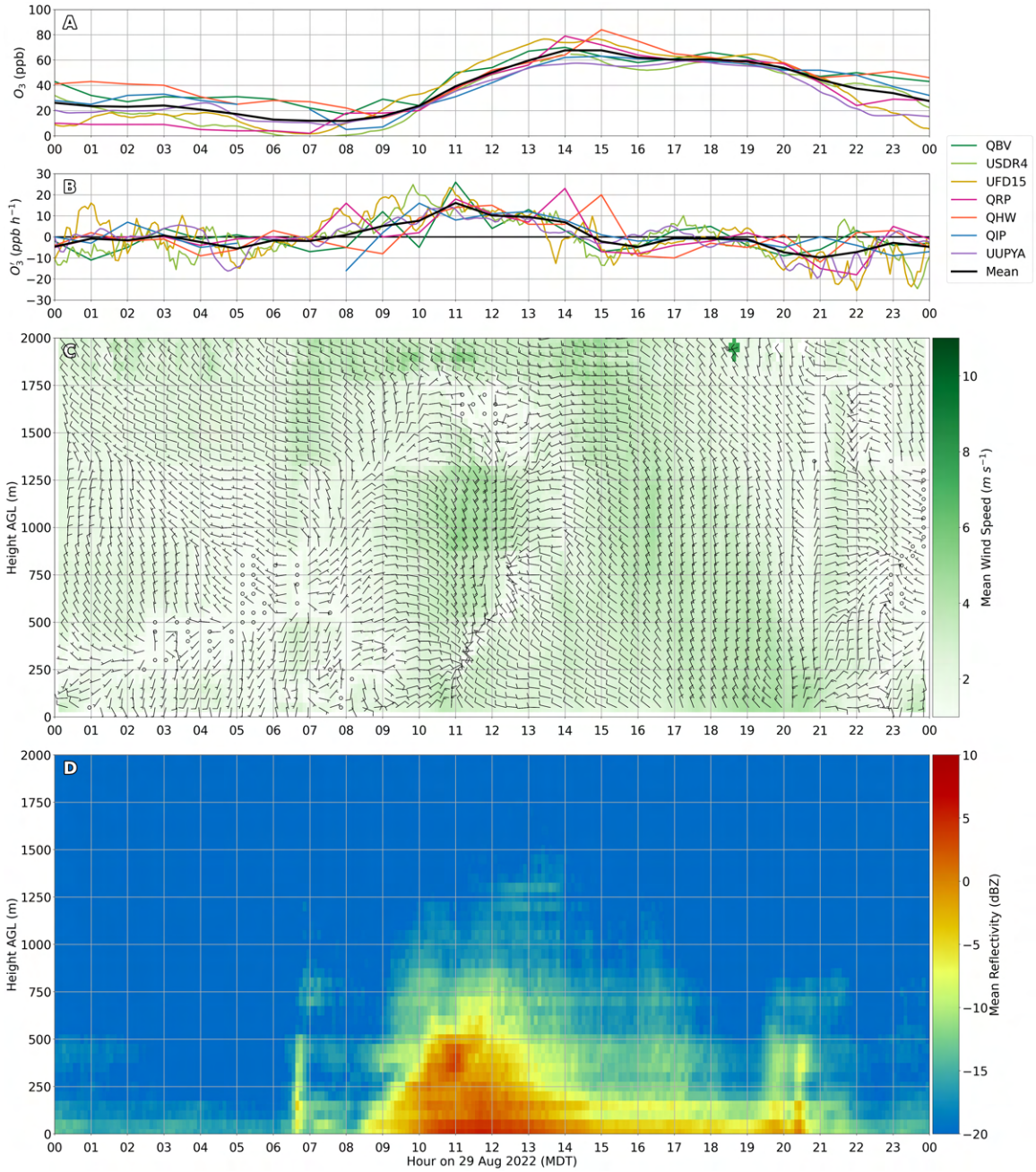

Figure 4.7: Surface observations and radar retrievals 29 Aug 2022. (a) O_3 (ppb) from DAQ and UU sites. (b) as in (a) except for O_3'. (c) TSLC VVP wind speed (fill) and wind barbs during 29 Aug 2022. Half (full) barbs correspond to 1.25 (2.5) $m\ s^{-1}$. (d) TSLC mean reflectivity RD-QVP (dBZ) during 29 Aug 2022.

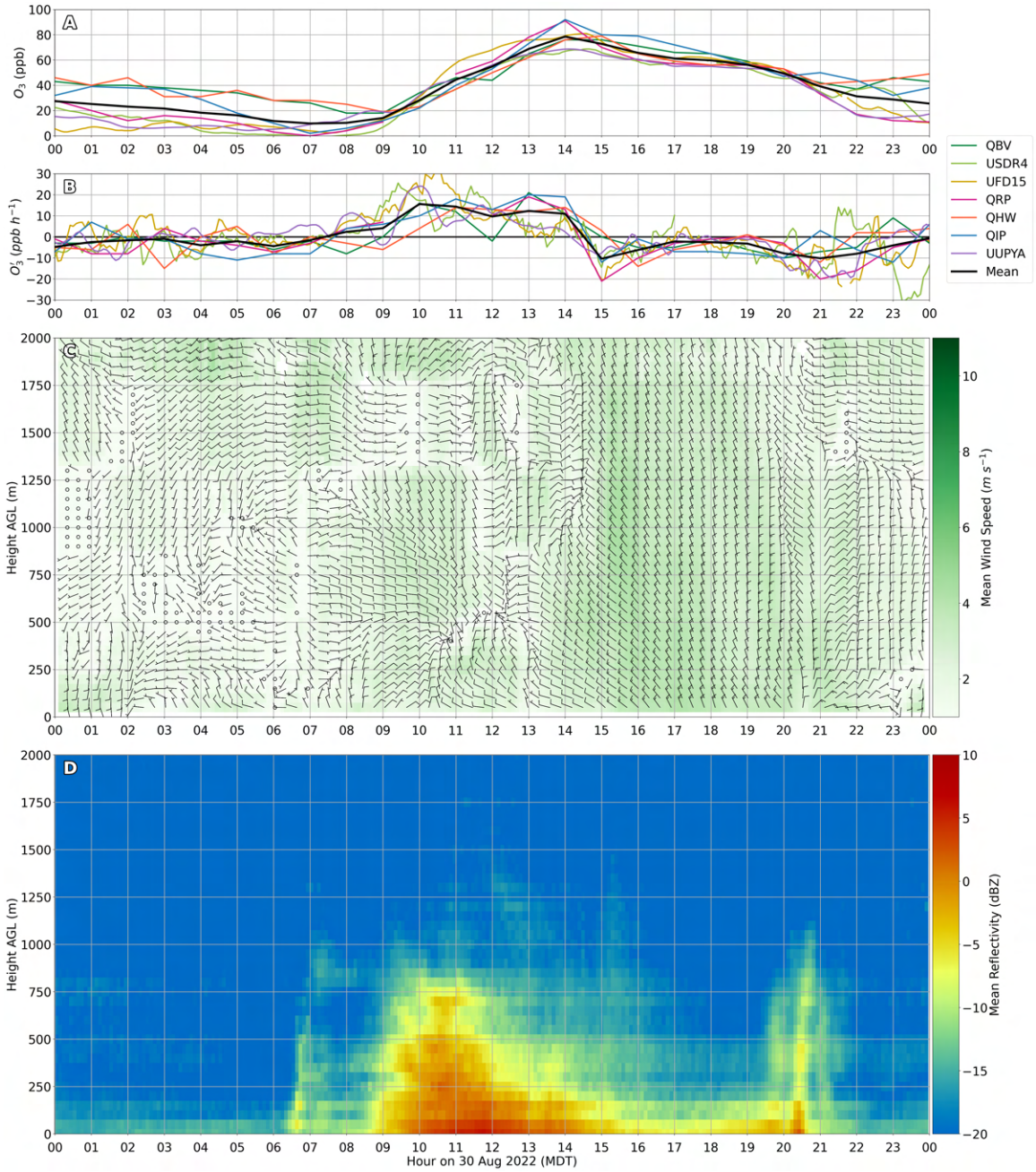

Figure 4.8: Surface observations and radar retrievals 30 Aug 2022. (a) O_3 (ppb) from DAQ and UU sites. (b) as in (a) except for O_3'. (c) TSLC VVP wind speed (fill) and wind barbs during 30 Aug 2022. Half (full) barbs correspond to 1.25 (2.5) $m\ s^{-1}$. (d) TSLC mean reflectivity RD-QVP (dBZ) during 30 Aug 2022.

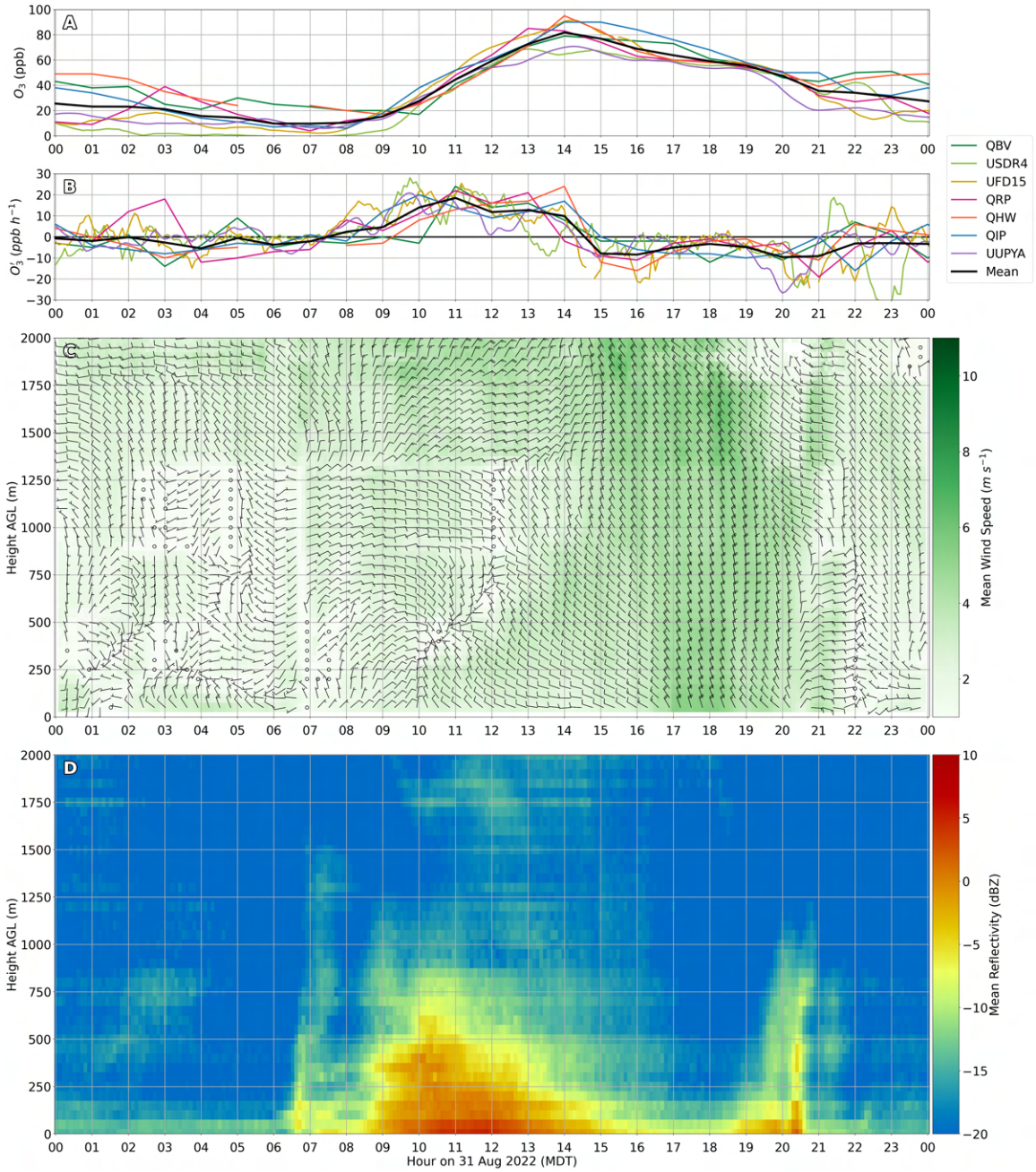

Figure 4.9: Surface observations and radar retrievals 31 Aug 2022. (a) O_3 (ppb) from DAQ and UU sites. (b) as in (a) except for O_3'. (c) TSLC VVP wind speed (fill) and wind barbs during 31 Aug 2022. Half (full) barbs correspond to 1.25 (2.5) $m\ s^{-1}$. (d) TSLC mean reflectivity RD-QVP (dBZ) during 31 Aug 2022.

(a)

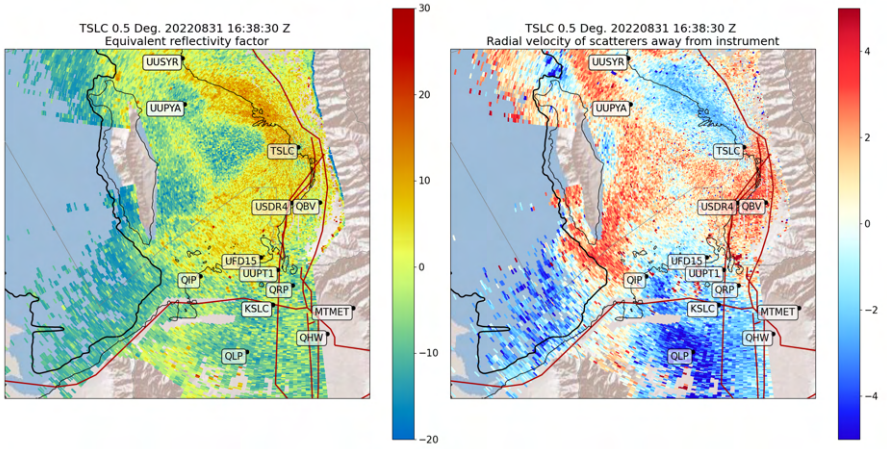

(b)

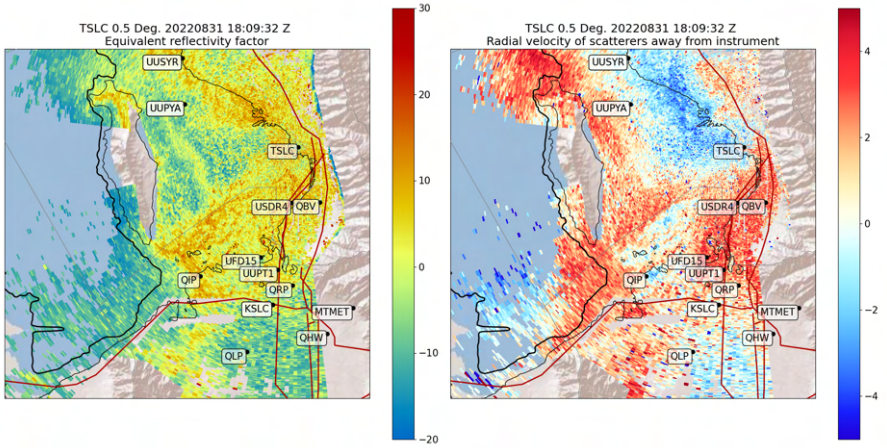

Figure 4.10: Plan view TSLC 0.5° imagery on 31 Aug 2022. (a) Left figure shows reflectivity (dBZ) at 1638 UTC. Right figure shows radial velocity ($m\ s^{-1}$) with blue indicating motion toward the radar and red indicating motion away according to the scale on the right. (b) as with (a) but at 1809 UTC. (c) as with (a) but at 2004 UTC. (d) as with (a) but at 2205 UTC. (e) as with (a) but at 2354 UTC.

(c)

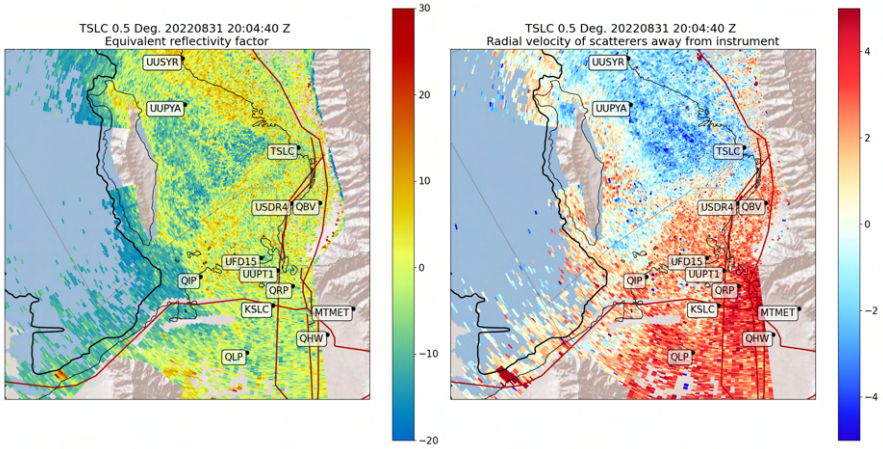

(d)

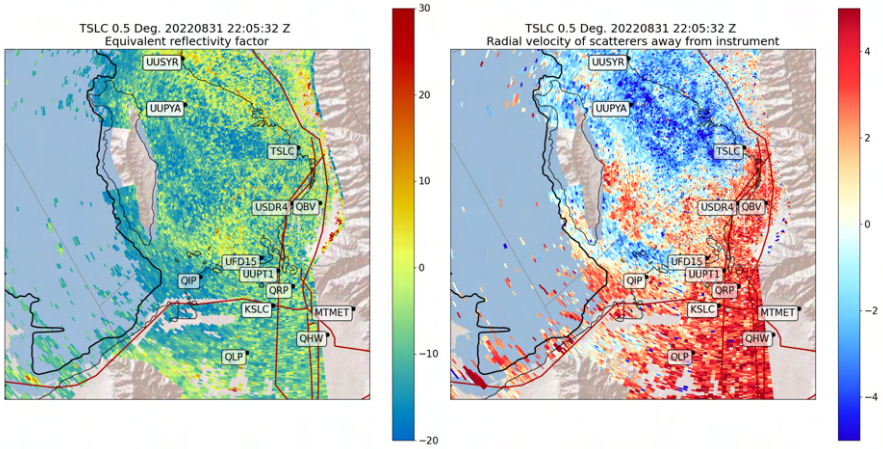

(e)

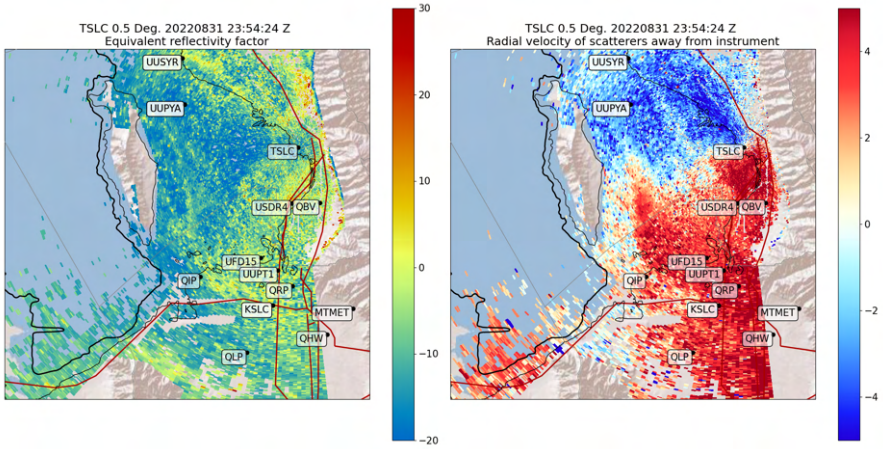

Figure 4.10 continued.

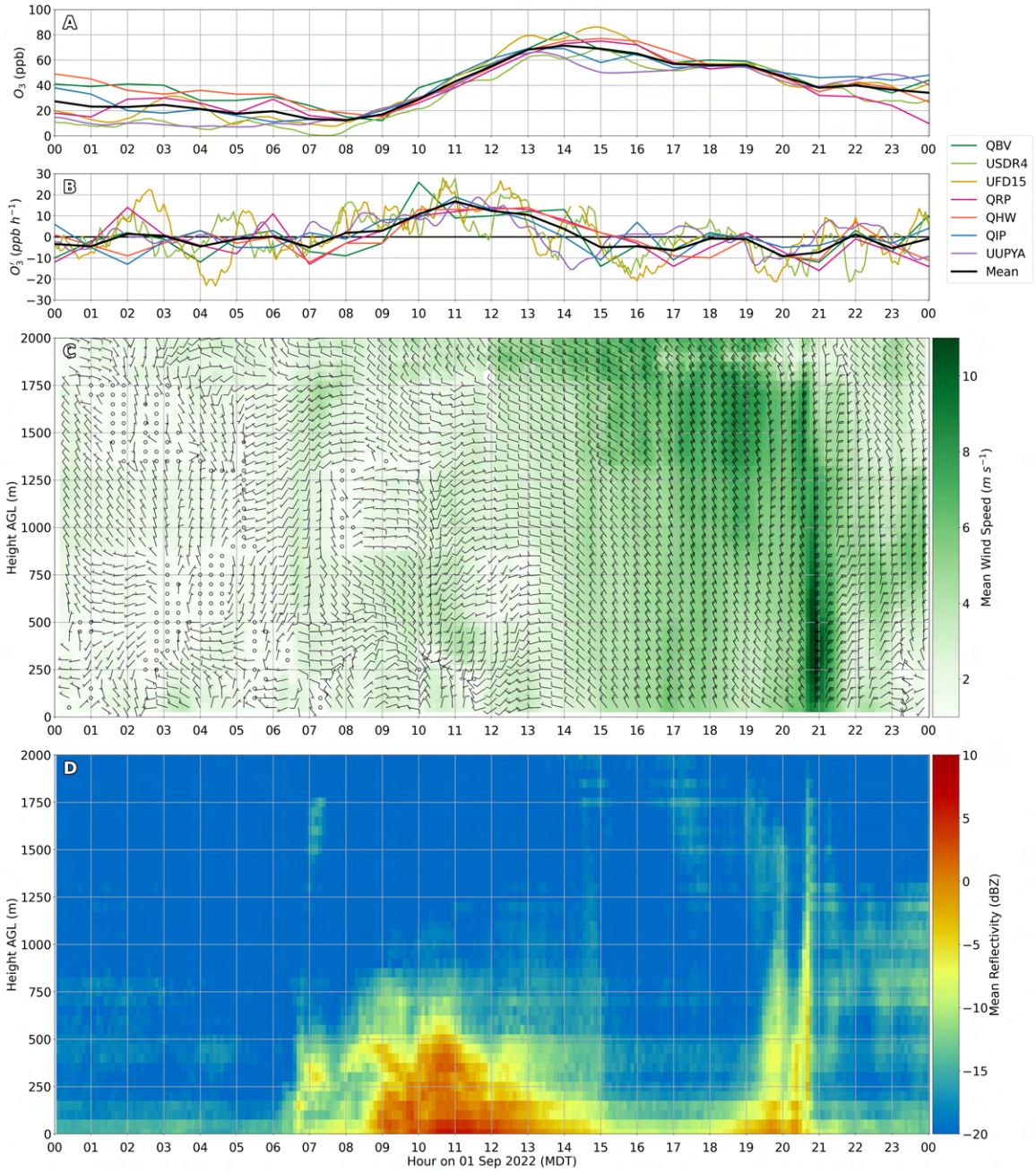

Figure 4.11: Surface observations and radar retrievals 01 Sep 2022. (a) O_3 (ppb) from DAQ and UU sites. (b) as in (a) except for O_3'. (c) TSLC VVP wind speed (fill) and wind barbs during 01 Sep 2022. Half (full) barbs correspond to 1.25 (2.5) $m\ s^{-1}$. (d) TSLC mean reflectivity RD-QVP (dBZ) during 01 Sep 2022.

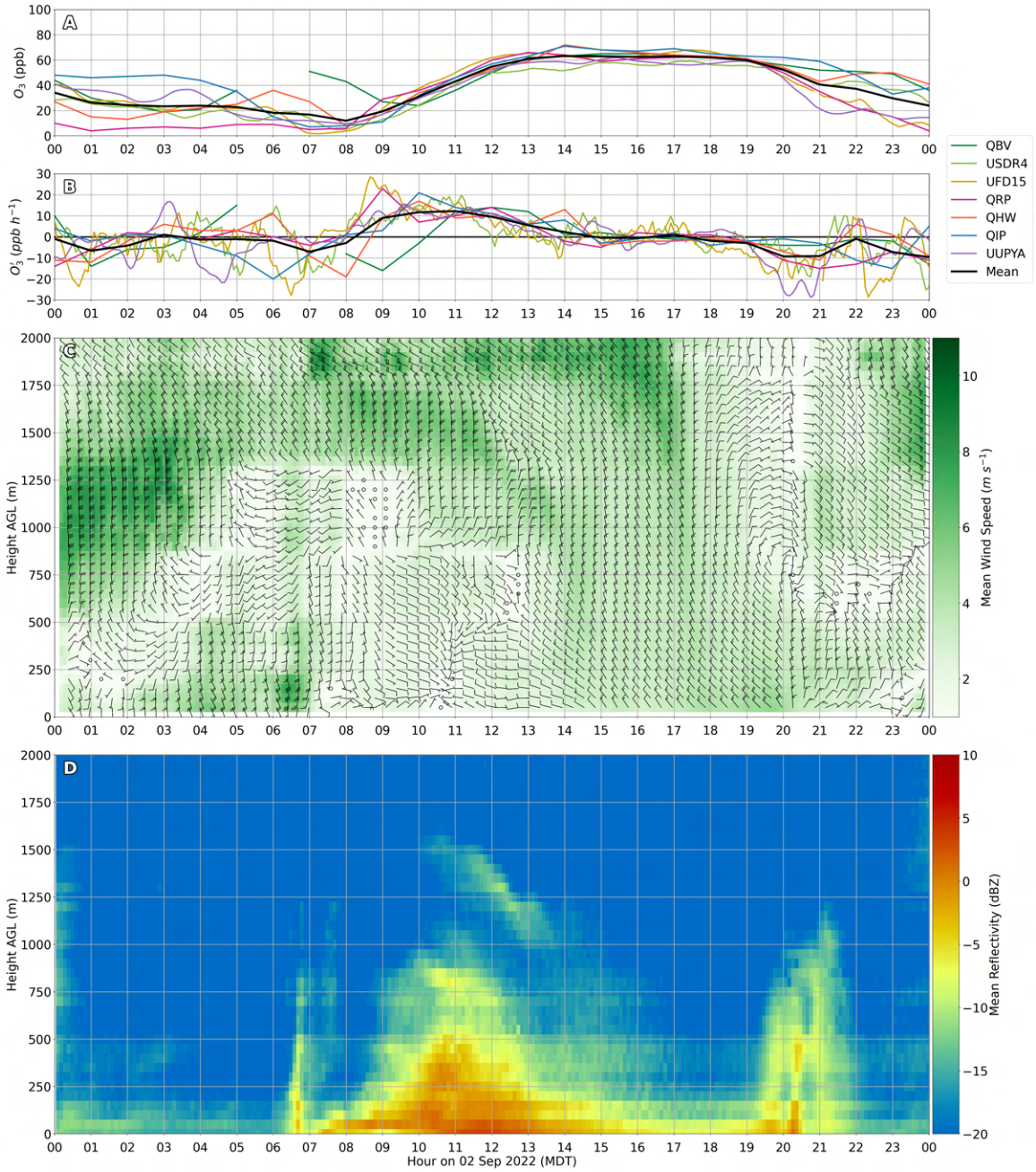

Figure 4.12: Surface observations and radar retrievals 02 Sep 2022. (a) O_3 (ppb) from DAQ and UU sites. (b) as in (a) except for O_3'. (c) TSLC VVP wind speed (fill) and wind barbs during 02 Sep 2022. Half (full) barbs correspond to 1.25 (2.5) $m\ s^{-1}$. (d) TSLC mean reflectivity RD-QVP (dBZ) during 02 Sep 2022.

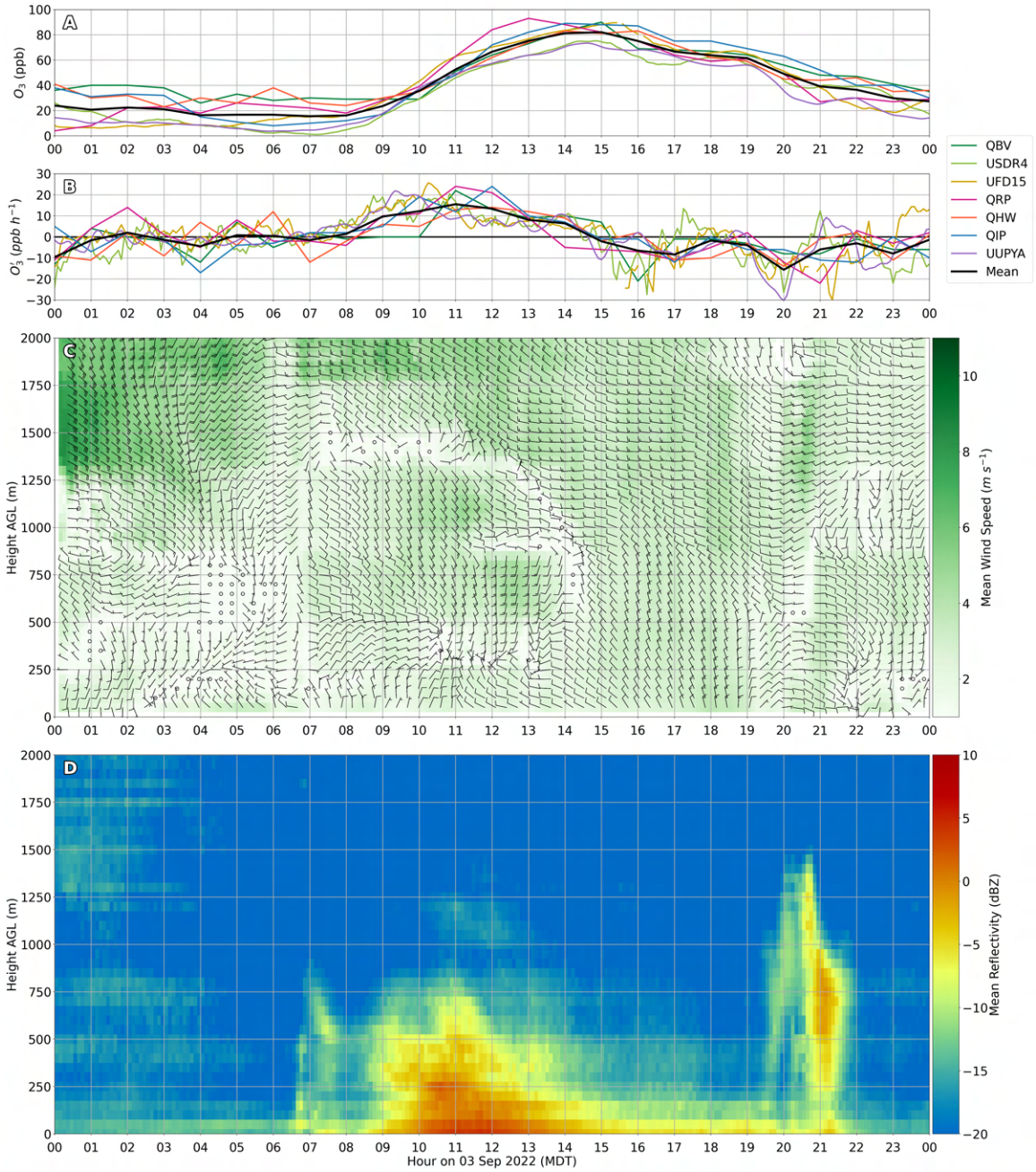

Figure 4.13: Surface observations and radar retrievals 03 Sep 2022. (a) O_3 (ppb) from DAQ and UU sites. (b) as in (a) except for O_3'. (c) TSLC VVP wind speed (fill) and wind barbs during 03 Sep 2022. Half (full) barbs correspond to 1.25 (2.5) $m\ s^{-1}$. (d) TSLC mean reflectivity RD-QVP (dBZ) during 03 Sep 2022.

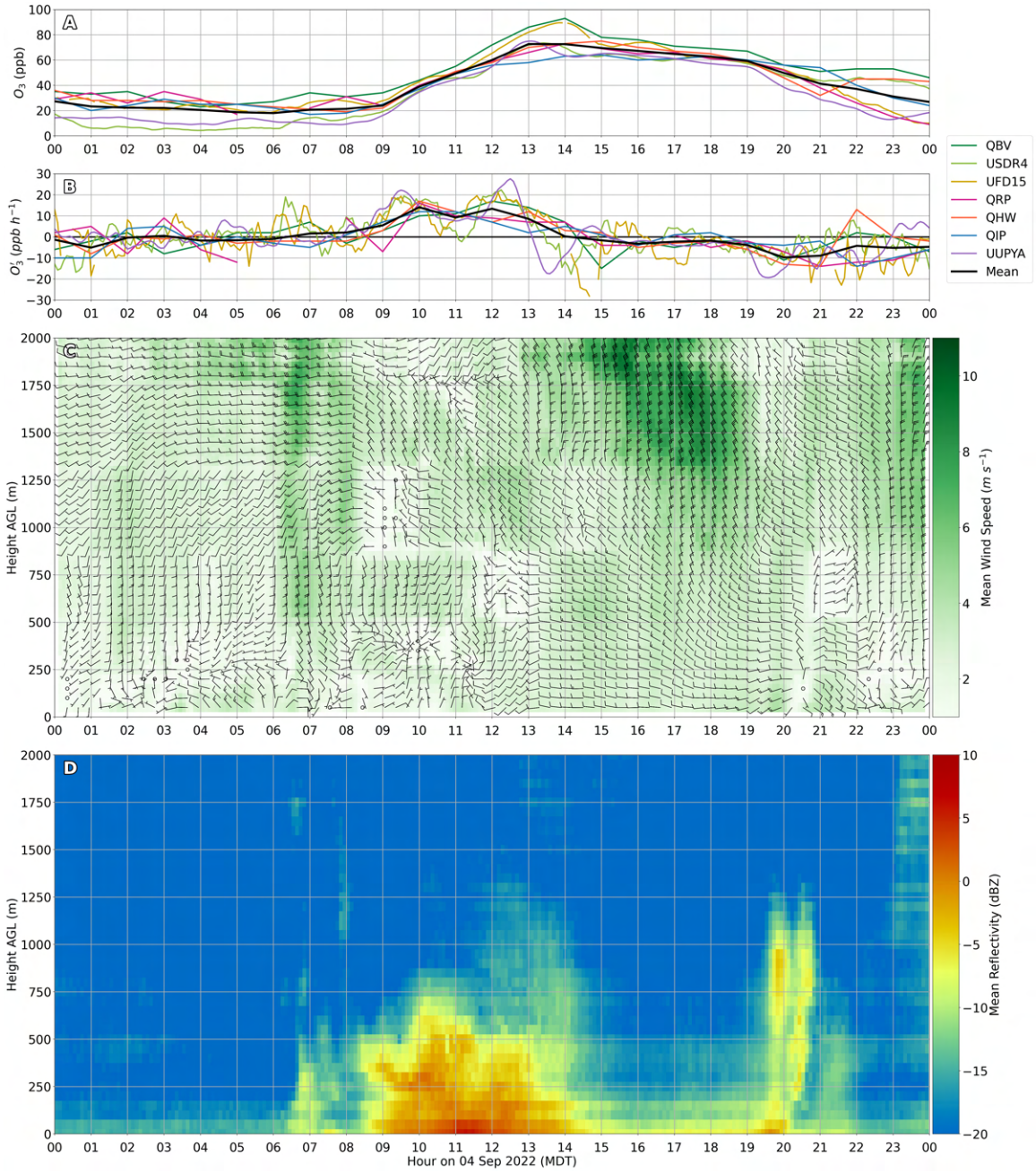

Figure 4.14: Surface observations and radar retrievals 04 Sep 2022. (a) O_3 (ppb) from DAQ and UU sites. (b) as in (a) except for O_3'. (c) TSLC VVP wind speed (fill) and wind barbs during 04 Sep 2022. Half (full) barbs correspond to 1.25 (2.5) $m\ s^{-1}$. (d) TSLC mean reflectivity RD-QVP (dBZ) during 04 Sep 2022.

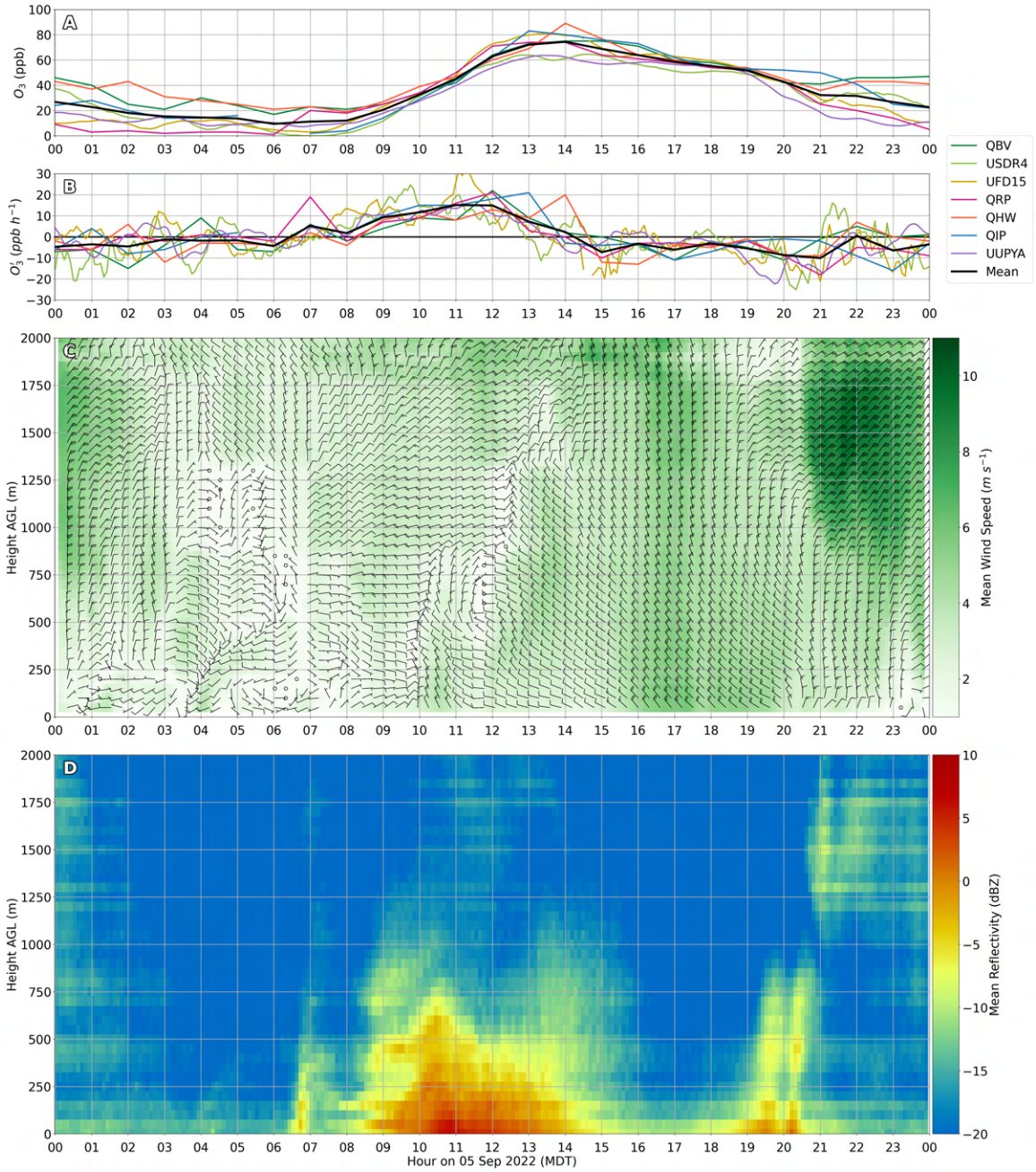

Figure 4.15: Surface observations and radar retrievals 05 Sep 2022. (a) O_3 (ppb) from DAQ and UU sites. (b) as in (a) except for O_3'. (c) TSLC VVP wind speed (fill) and wind barbs during 05 Sep 2022. Half (full) barbs correspond to 1.25 (2.5) $m\ s^{-1}$. (d) TSLC mean reflectivity RD-QVP (dBZ) during 05 Sep 2022.

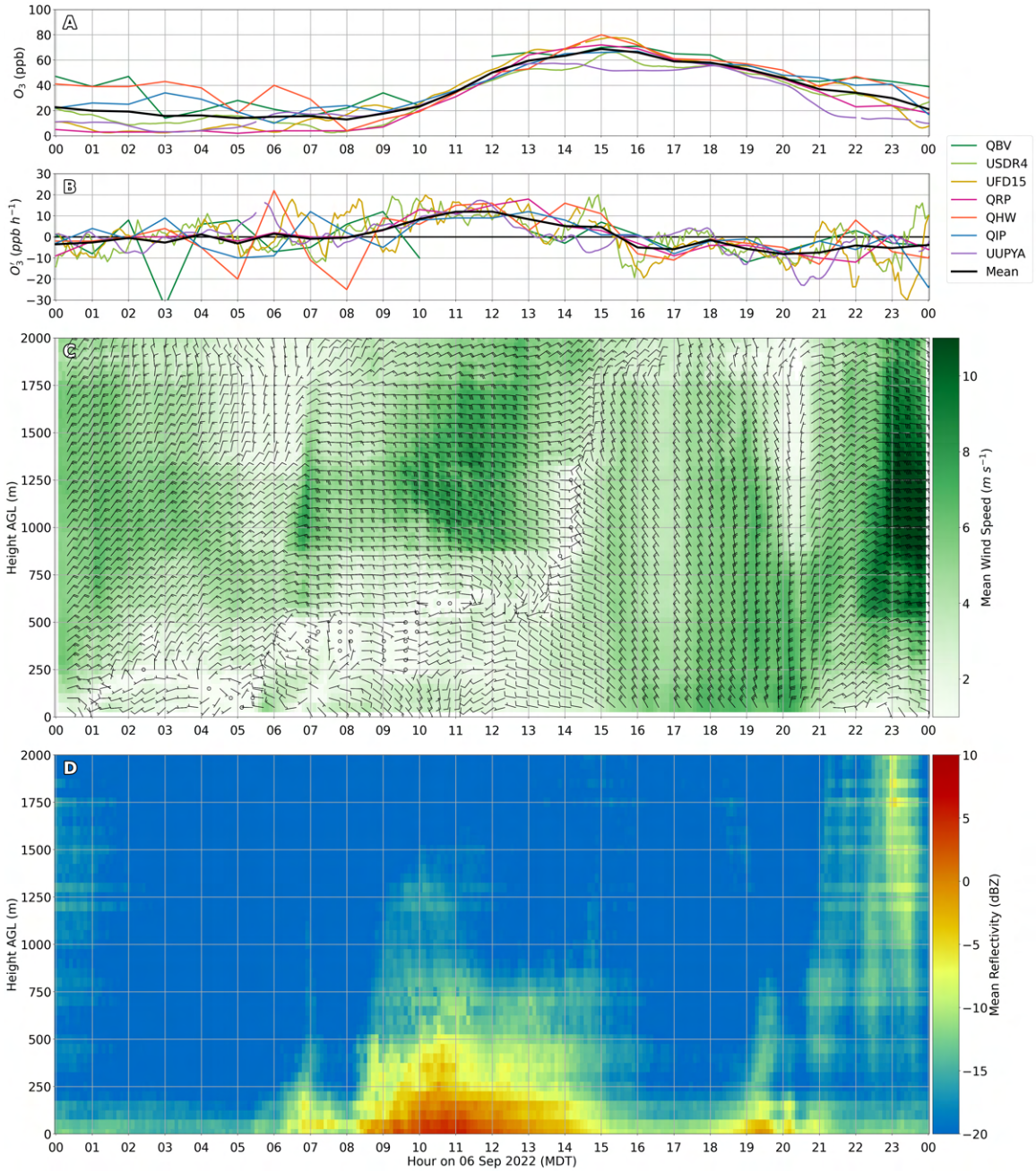

Figure 4.16: Surface observations and radar retrievals 06 Sep 2022. (a) O_3 (ppb) from DAQ and UU sites. (b) as in (a) except for O_3'. (c) TSLC VVP wind speed (fill) and wind barbs during 06 Sep 2022. Half (full) barbs correspond to 1.25 (2.5) $m\ s^{-1}$. (d) TSLC mean reflectivity RD-QVP (dBZ) during 06 Sep 2022.

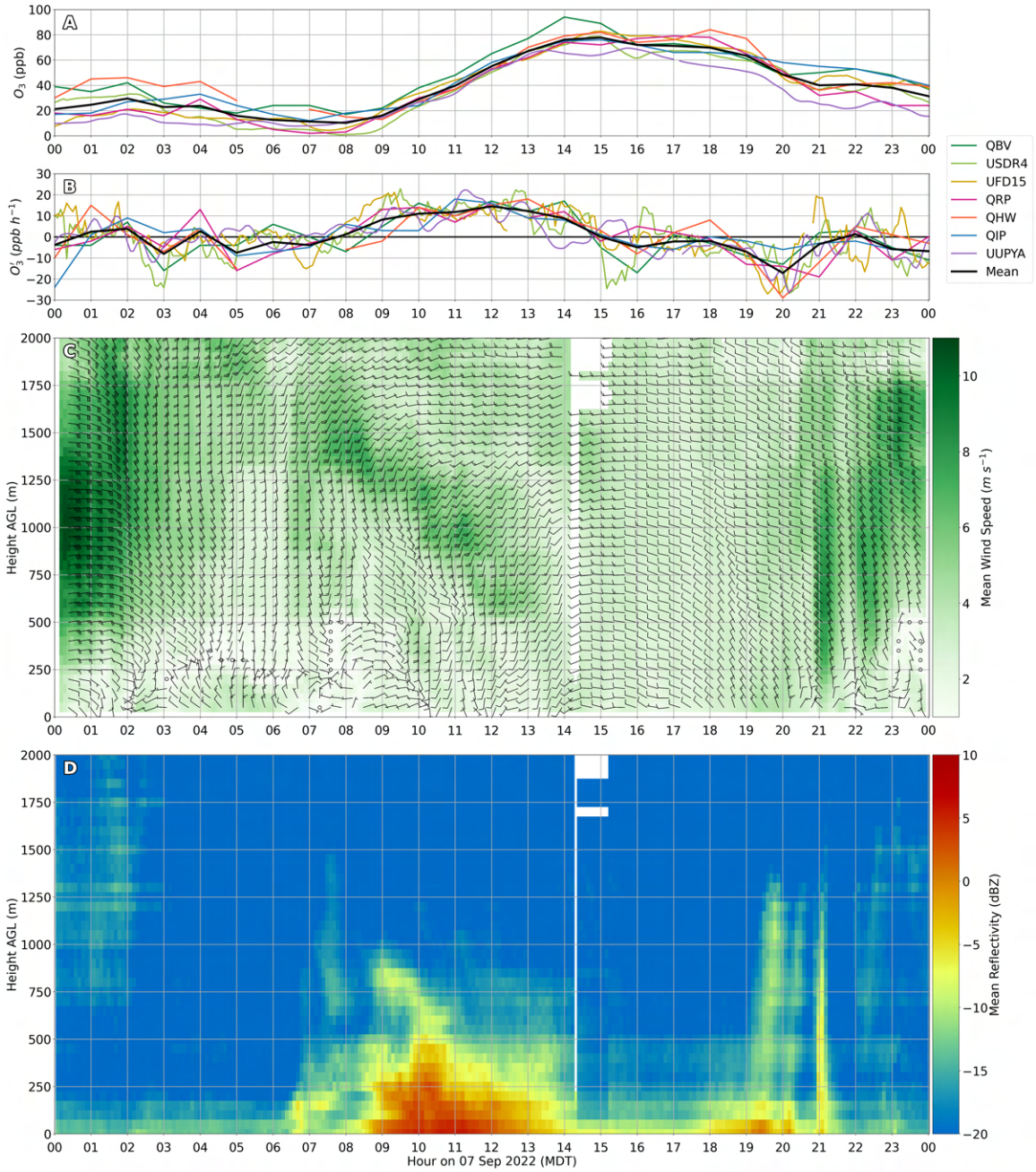

Figure 4.17: Surface observations and radar retrievals 07 Sep 2022. (a) O_3 (ppb) from DAQ and UU sites. (b) as in (a) except for O_3'. (c) TSLC VVP wind speed (fill) and wind barbs during 07 Sep 2022. Half (full) barbs correspond to 1.25 (2.5) $m\ s^{-1}$. (d) TSLC mean reflectivity RD-QVP (dBZ) during 07 Sep 2022.

CHAPTER 5

SUMMARY

The EPA classifies Salt Lake and Davis counties as being in moderate nonattainment towards meeting the current ozone standard. Much of the research related to ozone in northern Utah has focused on conditions in the urban SLV, yet O_3 in Davis County routinely is as high or higher there. Prior work has suggested that the higher concentrations measured at QBV in Davis County may arise from multiple factors including nearby sources of natural and industrial VOCs as well as terrain and boundary layer processes that may limit vertical and lateral mixing of ozone away from the region.

The objective of this study was to apply an under-utilized resource available in Davis County to examine the boundary layer in this region: output from the TSLC TDWR radar. Methods used previously on output from NEXRAD radars were applied and tested in order to examine winds and reflectivity at high temporal and vertical resolution within 5 km of the TSLC radar. Testing also involved examining output samples from TDWR radars at other locations, including those expected to be influenced by terrain effects (e.g., Las Vegas) and others that are not (e.g., Oklahoma City). In the case of TSLC, the horizontal extent was limited to 5 km in order to minimize terrain effects from the Wasatch Mountains to the east of the radar. TSLC wind profiles were compared to twice-daily profiles from rawinsondes launched at the SLC International Airport located 20 km to the south of TSLC and hourly profiles available from HRRR analyses. While the core features in the vertical wind profiles above 500 m during periods heavily influenced by local thermally-driven flows typically tend to agree among the three different data sets, substantial differences are often evident near the surface, particularly during the morning and during the critical transition from the stable to convective boundary layer during summer. The detail available from the TSLC radar to assess rapid wind shifts and locations of wind shear layers is invaluable, albeit

often applicable only close to the radar's location in Davis County and less representative of conditions in the SLV. However, plan view images at different elevation angles remain of high value for examining flow features (lake and playa breezes, outflow boundaries, and severe weather) beyond the SLC Airport into the SLV and north into Weber County.

Permanent and temporary equipment deployed for a 2022 summer field campaign were used to monitor O_3 concentrations from over the FBP, through the nearby wetlands, and into the urban corridor from Bountiful to Salt Lake City. It was beyond the scope of this study to take full advantage of all of those data resources for the entire summer season. Hence, focus was placed here on the O_3 monitored at seven sites during the ten-day LDP, in late August and early September when temperatures and O_3 were abnormally high. The large-scale conditions influencing this period were reviewed and then attention was placed on the average and individual daily evolution of O_3 and winds below 2000 m.

Commonly evident during all ten days was that O_3 is lowest near sunrise (0600-0700 MDT) and then rises sharply with increases of roughly 5-12 $ppb\ h^{-1}$ until after solar noon (1300 MDT). O_3 then decreases slowly after that time due to mixing within the CBL until sunset (1900-2000 MDT) after which becomes larger until after midnight. Similarly, weak winds tend to be present aloft in the 250-1250 m layer prior to sunrise and then transition to weak easterly flow after 0700 MDT. After 8 MDT, northeasterly-easterly winds below 250 m develop and then veer abruptly with time to westerly winds between 1000 and 1100 MDT. As the near-surface winds become westerly, the winds below 1000m become southerly. In addition, as the stable boundary layer weakens during the late morning and the CBL develops, this wind shear layer lifts rapidly by 1200 MDT to 1000m. By solar noon (1300 MDT), the CBL has deepened to higher than 2000m and the winds after that time are the strongest of the day from the northwest until sunset.

However, differences were present from day-to-day in the rate at which O_3 increased in the morning at the seven sites and times of peak concentration. These differences in O_3 concentrations at times were related in part to differences in the impacts of local thermally-driven flows (lake and playa breezes), mechanically-driven downslope winds, and transitory weather systems. The largest differences arise as a result of the multiple ways that surface inversions near TSLC transition to CBLs and how that affects the timing

for peak ozone concentrations in the region. Other factors include background ozone concentrations that are mixed vertically with the ozone produced near the surface within the CBL as well as inserted into the near-surface layer at night through boundary layer flows. Omitted from discussion here was the high O_3 during 9-12 Sep that was heavily influenced by regional transport of wildfire smoke.

The boundary layer and air chemistry monitoring resources available in the SLV and FBP exceed that available in most urban areas. However, the techniques developed here could be readily applied to other regions impacted by high O_3 where either NEXRAD or TDWR radars are located. While the high base elevation of the SLC NEXRAD limited its usefulness for this study, using the additional polarimetric data for profiles of boundary layer development at other locations would be of great utility and could potentially lead to a nationwide survey of boundary layer conditions and ozone during all seasons. TDWR radar output in Denver, Phoenix, and Las Vegas could be examined for these locations that also routinely exceed EPA ozone standards and are influenced by complex terrain. Since TDWR velocity data is not currently integrated into NCEP operational data assimilations, VVPs from the TDWR radars can be used to validate and improve boundary layer parameterizations, especially at sites in complex terrain. In addition, large-eddy simulations are increasingly used for examining boundary layer circulations that could be validated using the routine high spatial and temporal wind profiles available from the TDWR network. Developing VVP and RD-QVP retrievals to taper by horizontal range during calculations as done by Tobin and Kumjian (2017) could assist with reducing the discontinuities in the retrieval, opening the possibility to use a gradient based method to quantitatively track CBL evolution. Near-surface resolution could also be feasibly increased due to higher near-surface data density by using non-constant bin spacing.

A number of questions remain open within the FBP and SLV basins. The repeatability of the signals seen in these case studies can be tested using other days, especially as the record becomes more substantial in the future. Since TSLC and KMTX are significantly offset from each other and KMTX scans above TSLC, dual doppler analysis using both radars can be done to examine the spatial extent of the features seen in this study. The depth of the boundary layer near TSLC is not constant and strongly influenced by the

surrounding terrain. Splitting the scanning domain of TSLC based on the presence of mountains and carrying out RD-QVP retrievals over just those sectors could be used to characterize boundary layer growth over the SLC airport or over the mountain slopes relative to the basin floor. Blowing dust from the GSL playa is a significant environmental concern within the FBP and SLV urban corridors, and TSLC is oftentimes sensitive enough to pick up dust emissions. Work is ongoing using TSLC and dust monitoring equipment at UUPYA to examine these signals.

REFERENCES

Bachmann, S., and D. Zrnić, 2007: Spectral density of polarimetric variables separating biological scatterers in the VAD display. *J. Atmos. Oceanic Technol.*, **24 (7)**, 1186–1198, doi:10.1175/JTECH2043.1.

Baier, B. C., W. H. Brune, B. L. Lefer, D. O. Miller, and D. K. Martins, 2015: Direct ozone production rate measurements and their use in assessing ozone source and receptor regions for Houston in 2013. *Atmos. Environ.*, **114**, 83–91, doi:10.1016/j.atmosenv.2015.05.033.

Banghoff, J. R., D. J. Stensrud, and M. R. Kumjian, 2018: Convective boundary layer depth estimation from S-Band dual-polarization radar. *J. Atmos. Oceanic Technol.*, **35 (8)**, 1723–1733, doi:10.1175/JTECH-D-17-0210.1.

Banta, R. M., and Coauthors, 2011: Dependence of daily peak O_3 concentrations near Houston, Texas on environmental factors: Wind speed, temperature, and boundary-layer depth. *Atmos. Environ.*, **45 (1)**, 162–173, doi:10.1016/j.atmosenv.2010.09.030.

Banta, R. M., and Coauthors, 2020: Characterizing NWP model errors using Doppler-lidar measurements of recurrent regional diurnal flows: Marine-air intrusions into the Columbia River Basin. *Mon. Wea. Rev.*, **148 (3)**, 929–953, doi:10.1175/MWR-D-19-0188.1.

Benjamin, S. G., and Coauthors, 2016: A North American hourly assimilation and model forecast cycle: The Rapid Refresh. *Mon. Wea. Rev.*, **144 (4)**, 1669–1694, doi:10.1175/MWR-D-15-0242.1.

Blaylock, B. K., J. D. Horel, and E. T. Crosman, 2017: Impact of lake breezes on summer ozone concentrations in the Salt Lake Valley. *J. Appl. Meteor. Climatol.*, **56 (2)**, 353–370, doi:10.1175/JAMC-D-16-0216.1.

Boccippio, D. J., 1995: A diagnostic analysis of the VVP single-Doppler retrieval technique. *J. Atmos. Oceanic Technol.*, **12 (2)**, 230–248, doi:10.1175/1520-0426(1995)012<0230:ADAOTV>2.0.CO;2.

Brodin, M., D. Helmig, and S. Oltmans, 2010: Seasonal ozone behavior along an elevation gradient in the Colorado Front Range Mountains. *Atmos. Environ.*, **44 (39)**, 5305–5315, doi:10.1016/j.atmosenv.2010.06.033.

Browning, K. A., and R. Wexler, 1968: The determination of kinematic properties of a wind field using Doppler radar. *J. Appl. Meteor. Climatol.*, **7 (1)**, 105–113, doi:10.1175/1520-0450(1968)007<0105:TDOKPO>2.0.CO;2.

Cho, J. Y. N., 2005: Multi-PRI signal processing for the Terminal Doppler Weather Radar. Part II: Range–velocity ambiguity mitigation. *J. Atmos. Oceanic Technol.*, **22 (10)**, 1507–1519, doi:10.1175/JTECH1805.1.

Cho, J. Y. N., 2010: Signal processing algorithms for the Terminal Doppler Weather Radar: Build 2. Tech. Rep. ATC-363, MIT Lincoln Laboratory. 89 pp.

Chow, F. K., S. F. De Wekker, and B. J. Snyder, Eds., 2013: *Mountain Weather Research and Forecasting*. Springer Netherlands, 750 pp., doi:10.1007/978-94-007-4098-3.

Chrust, M. F., C. D. Whiteman, and S. W. Hoch, 2013: Observations of thermally driven wind jets at the exit of Weber Canyon, Utah. *J. Appl. Meteor. Climatol.*, **52 (5)**, 1187–1200, doi:10.1175/JAMC-D-12-0221.1.

Clifton, O. E., and Coauthors, 2020: Dry deposition of ozone over land: Processes, measurement, and modeling. *Rev. Geophys.*, **58 (1)**, e2019RG000 670, doi:10.1029/2019RG000670.

Coates, J., K. A. Mar, N. Ojha, and T. M. Butler, 2016: The influence of temperature on ozone production under varying NO_x conditions: A modelling study. *Atmos. Chem. Phys.*, **16 (18)**, 11 601–11 615, doi:10.5194/acp-16-11601-2016.

Crosman, E. T., and J. D. Horel, 2010: Sea and lake breezes: A review of numerical studies. *Boundary Layer Meteorol.*, **137 (1)**, 1–29, doi:10.1007/s10546-010-9517-9.

Doviak, R. J., and D. S. Zrnic, 1993: *Doppler Weather Radar and Weather Observations*. 2nd ed., Dover Publications, Inc., 562 pp.

Dowell, D. C., and Coauthors, 2022: The high-resolution rapid refresh (HRRR): An hourly updating convection-allowing forecast model. Part I: Motivation and system description. *Wea. Forecasting*, **37 (8)**, 1371–1395, doi:10.1175/WAF-D-21-0151.1.

Fann, N., A. D. Lamson, S. C. Anenberg, K. Wesson, D. Risley, and B. J. Hubbell, 2012: Estimating the national public health burden associated with exposure to ambient $PM_{2.5}$ and ozone. *Risk Anal.*, **32 (1)**, 81–95, doi:10.1111/j.1539-6924.2011.01630.x.

Goldberg, D. L., C. P. Loughner, M. Tzortziou, J. W. Stehr, K. E. Pickering, L. T. Marufu, and R. R. Dickerson, 2014: Higher surface ozone concentrations over the Chesapeake Bay than over the adjacent land: Observations and models from the DISCOVER-AQ and CBODAQ campaigns. *Atmos. Environ.*, **84**, 9–19, doi:10.1016/j.atmosenv.2013.11.008.

Gowan, T. A., J. D. Horel, A. A. Jacques, and A. Kovac, 2022: Using cloud computing to analyze model output archived in Zarr format. *J. Atmos. Oceanic Technol.*, **39 (4)**, 449–462, doi:10.1175/JTECH-D-21-0106.1.

Griffin, E. M., T. J. Schuur, and A. V. Ryzhkov, 2018: A polarimetric analysis of ice microphysical processes in snow, using quasi-vertical profiles. *J. Appl. Meteor. Climatol.*, **57 (1)**, 31 – 50, doi:10.1175/JAMC-D-17-0033.1.

Heinselman, P. L., P. L. Spencer, K. L. Elmore, D. J. Stensrud, R. M. Hluchan, and P. C. Burke, 2009: Radar reflectivity–based estimates of mixed layer depth. *J. Atmos. Oceanic Technol.*, **26 (2)**, 229–239, doi:10.1175/2008JTECHA1091.1.

Holleman, I., 2005: Quality control and verification of weather radar wind profiles. *J. Atmos. Oceanic Technol.*, **22 (10)**, 1541–1550, doi:10.1175/JTECH1781.1.

Horel, J., E. Crosman, A. Jacques, B. Blaylock, S. Arens, A. Long, J. Sohl, and R. Martin, 2016: Summer ozone concentrations in the vicinity of the Great Salt Lake. *Atmos. Sci. Lett.*, **17 (9)**, 480–486, doi:10.1002/asl.680.

Horel, J. D., S. W. Hoch, A. Jacques, and C. Johnson, 2023: Impacts of the Great Salt Lake on summer ozone concentrations along the Wasatch Front. Tech. rep., Utah Division of Air Quality, 36 pp.

Hu, J., and A. Ryzhkov, 2022: Climatology of the vertical profiles of polarimetric radar variables and retrieved microphysical parameters in continental/tropical MCSs and landfalling hurricanes. *J. Geophys. Res.*, **127 (5)**, e2021JD035 498, doi:10.1029/2021jd035498.

Hubbell, B. J., A. Hallberg, D. R. McCubbin, and E. Post, 2005: Health-related benefits of attaining the 8-hr ozone standard. *Environ. Health Perspect.*, **113 (1)**, 73–82, doi:10.1289/ehp.7186.

Jaffe, D., 2011: Relationship between surface and free tropospheric ozone in the Western U.S. *Environ. Sci. Technol.*, **45 (2)**, 432–438, doi:10.1021/es1028102.

James, E. P., and Coauthors, 2022: The High-Resolution Rapid Refresh (HRRR): An hourly updating convection-allowing forecast model. Part II: Forecast performance. *Wea. Forecasting*, **37 (8)**, 1397–1417, doi:10.1175/WAF-D-21-0130.1.

Kaser, L., and Coauthors, 2017: The effect of entrainment through atmospheric boundary layer growth on observed and modeled surface ozone in the Colorado Front Range. *J. Geophys. Res. Atmos.*, **122 (11)**, 6075–6093, doi:10.1002/2016JD026245.

Kristianti, F., J. Dujardin, F. Gerber, H. Huwald, S. W. Hoch, and M. Lehning, 2023: Combining weather station data and short-term LiDAR deployment to estimate wind energy potential with machine learning: A case study from the Swiss Alps. *Boundary Layer Meteorol.*, **188 (1)**, 185–208, doi:10.1007/s10546-023-00808-y.

Lhermitte, R. M., and D. Atlas, 1961: Precipitation motion by pulse Doppler radar. *Proc. Ninth Weather Radar Conf.*, Kansas City, MO, Amer. Meteor. Soc., 218-223.

Liu, S., and Coauthors, 2016: WSR-88D Radar data processing at NCEP. *Wea. Forecasting*, **31 (6)**, 2047–2055, doi:10.1175/WAF-D-16-0003.1.

Liu, S. C., and Coauthors, 1992: A study of the photochemistry and ozone budget during the Mauna Loa Observatory Photochemistry Experiment. *J. Geophys. Res. Atmos.*, **97 (D10)**, 10 463–10 471, doi:10.1029/91JD02298.

Massey, J. D., W. J. Steenburgh, S. W. Hoch, and D. D. Jensen, 2017: Simulated and observed surface energy fluxes and resulting playa breezes during the MATERHORN field campaigns. *J. Appl. Meteor. Climatol.*, **56 (4)**, 915–935, doi:10.1175/JAMC-D-16-0161.1.

Matejka, T., and R. C. Srivastava, 1991: An improved version of the extended velocity-azimuth display analysis of single-Doppler radar data. *J. Atmos. Oceanic Technol.*, **8 (4)**, 453–466, doi:10.1175/1520-0426(1991)008<0453:AIVOTE>2.0.CO;2.

NOAA Information Technology, 2023: NOAA Open Data Dissemination Program. https://www.noaa.gov/information-technology/open-data-dissemination, Accessed 6 Sep 2023.

NOAA NCEI, 2022a: August 2022 national climate report. https://www.ncei.noaa.gov/access/monitoring/monthly-report/national/202208, Accessed 6 Sep 2023.

NOAA NCEI, 2022b: September 2022 national climate report. https://www.ncei.noaa.gov/access/monitoring/monthly-report/national/202209, Accessed 6 Sep 2023.

NOAA NCEI, 2023a: Next Generation Weather Radar (NEXRAD). https://www.ncei.noaa.gov/products/radar/next-generation-weather-radar, Accessed 6 Sep 2023.

NOAA NCEI, 2023b: Terminal Doppler Weather Radar (TDWR). https://www.ncei.noaa.gov/products/radar/terminal-doppler-weather-radar, Accessed 6 Sep 2023.

NOAA NCEP EMC, 2021: High resolution rapid refresh. https://www.emc.ncep.noaa.gov/emc/pages/numerical_forecast_systems/hrrr.php, Accessed 6 Sep 2023.

Pichugina, Y. L., and Coauthors, 2019: Spatial variability of winds and HRRR–NCEP model error statistics at three Doppler-lidar sites in the wind-energy generation region of the Columbia River Basin. *J. Appl. Meteor. Climatol.*, **58 (8)**, 1633–1656, doi:10.1175/JAMC-D-18-0244.1.

Pusede, S. E., A. L. Steiner, and R. C. Cohen, 2015: Temperature and recent trends in the chemistry of continental surface ozone. *Chem. Rev.*, **115 (10)**, 3898–3918, doi:10.1021/cr5006815.

Ryzhkov, A., P. Zhang, H. Reeves, M. Kumjian, T. Tschallener, S. Trömel, and C. Simmer, 2016: Quasi-vertical profiles—A new way to look at polarimetric radar data. *J. Atmos. Oceanic Technol.*, **33 (3)**, 551–562, doi:10.1175/JTECH-D-15-0020.1.

Schwiesow, R. L., P. Köpp, and C. Werner, 1985: Comparison of CW-lidar-measured wind values obtained by full conical scan, conical sector scan and two-point techniques. *J. Atmos. Oceanic Technol.*, **2 (1)**, 3–14, doi:10.1175/1520-0426(1985)002<0003:COCLMW>2.0.CO;2.

Seinfeld, J. H., and S. N. Pandis, 2016: *Atmospheric Chemistry and Physics: From Air Pollution to Climate Change*. 3rd ed., Wiley, 1149 pp.

Shenghui, Z., W. Ming, W. Lijun, Z. Chang, and Z. Mingxu, 2014: Sensitivity analysis of the VVP wind retrieval method for single-Doppler weather radars. *J. Atmos. Oceanic Technol.*, **31 (6)**, 1289–1300, doi:10.1175/JTECH-D-13-00190.1.

Simpson, W. R., and Coauthors, 2007: Halogens and their role in polar boundary-layer ozone depletion. *Atmos. Chem. Phys.*, **7 (16)**, 4375–4418, doi:10.5194/acp-7-4375-2007.

Smith, T. M., and Coauthors, 2016: Multi-radar multi-sensor (MRMS) severe weather and aviation products: Initial operating capabilities. *Bull. Amer. Meteor. Soc.*, **97 (9)**, 1617–1630, doi:10.1175/BAMS-D-14-00173.1.

Sousa, S. I. V., M. C. M. Alvim-Ferraz, and F. G. Martins, 2013: Health effects of ozone focusing on childhood asthma: What is now known – A review from an epidemiological point of view. *Chemosphere*, **90 (7)**, 2051–2058, doi:10.1016/j.chemosphere.2012.10.063.

Stull, R. B., 1988: *An Introduction to Boundary Layer Meteorology*. Kluwer Academic Publishers, 666 pp.

Teschke, G., and V. Lehmann, 2017: Mean wind vector estimation using the velocity–azimuth display (VAD) method: An explicit algebraic solution. *Atmos. Meas. Tech.*, **10 (9)**, 3265–3271, doi:10.5194/amt-10-3265-2017.

Tobin, D. M., and M. R. Kumjian, 2017: Polarimetric radar and surface-based precipitation-type observations of ice pellet to freezing rain transitions. *Wea. Forecasting*, **32 (6)**, 2065–2082, doi:10.1175/WAF-D-17-0054.1.

Van Dingenen, R., F. J. Dentener, F. Raes, M. C. Krol, L. Emberson, and J. Cofala, 2009: The global impact of ozone on agricultural crop yields under current and future air quality legislation. *Atmos. Environ.*, **43 (3)**, 604–618, doi:10.1016/j.atmosenv.2008.10.033.

Waldteufel, P., and H. Corbin, 1979: On the analysis of single-Doppler radar data. *J. Appl. Meteor. Climatol.*, **18 (4)**, 532–542, doi:10.1175/1520-0450(1979)018<0532:OTAOSD>2.0.CO;2.

Wang, H., R. J. Barthelmie, A. Clifton, and S. C. Pryor, 2015: Wind measurements from arc scans with Doppler wind lidar. *J. Atmos. Oceanic Technol.*, **32 (11)**, 2024–2040, doi:10.1175/JTECH-D-14-00059.1.

Wentworth, G. R., J. G. Murphy, and D. M. L. Sills, 2015: Impact of lake breezes on ozone and nitrogen oxides in the Greater Toronto Area. *Atmos. Environ.*, **109**, 52–60, doi:10.1016/j.atmosenv.2015.03.002.

Wildmann, N., E. Päschke, A. Roiger, and C. Mallaun, 2020: Towards improved turbulence estimation with Doppler wind lidar velocity-azimuth display (VAD) scans. *Atmos. Meas. Tech.*, **13 (8)**, 4141–4158, doi:10.5194/amt-13-4141-2020.

Zhang, J., and Coauthors, 2016: Multi-radar multi-sensor (MRMS) quantitative precipitation estimation: Initial operating capabilities. *Bull. Amer. Meteor. Soc.*, **97 (4)**, 621–638, doi:10.1175/BAMS-D-14-00174.1.

Zrnic, D., and A. Ryzhkov, 1998: Observations of insects and birds with a polarimetric radar. *IEEE Trans. Geosci. Remote Sens.*, **36 (2)**, 661–668, doi:10.1109/36.662746.

Zumpfe, D. E., and J. D. Horel, 2007: Lake-breeze fronts in the Salt Lake Valley. *J. Appl. Meteor. Climatol.*, **46 (2)**, 196–211, doi:10.1175/JAM2449.1.